This article has been accepted for publication in IEEE Transactions on Transportation Electrification. This is the author's version which has not been fully edited and content may change prior to final publication. Citation information: DOI 10.1109/TTE.2023.3301549

Synthesis of Consequent Pole Vernier Permanent Magnet Machine Based on Oscillating Magnetic Potential Difference Model

Li Fang[1], *Yuanzhi Zhang[2], *Member*, *IEEE*, Dawei Li[1], *Senior Member*, *IEEE*, Tianjie Zou[3], *Member*, *IEEE*

[1] School of Electrical and Electronic Engineering, Huazhong University of Science and Technology, Wuhan 430070, China

[2] Hubei Key Laboratory of Power Equipment & System Security for Integrated Energy, School of Electrical Engineering and Automation, Wuhan University, Wuhan 430070, China

[3] Power Electronics, Machines and Control (PEMC) Group, University of Nottingham, NG7 2RD, Nottingham, UK

Email: d202080539@hust.edu.cn; yz_zhang@whu.edu.cn; daweili@hust.edu.cn; Tianjie.Zou@nottingham.ac.uk

***Abstract*—In recent years, consequent pole vernier permanent magnet machine (CPVPMM) has been found higher torque capability and less magnet usage compared to the surface-mounted counterpart i.e. SVPMM, thus attracting extensive interests. Meanwhile, the theoretical basis of CPVPMM is not well established because of its unconventional PM arrangement. Due to the simplified dual-salient permeance model widely adopted in CPVPMM, the misinterpretation in time-space distribution of magnetizing magnetomotive force (MMF) and air-gap permeance leads to deviated sizing equations, which hinders the development of CPVPMM. This paper proposes a new analytical model, i.e. the magnetic potential difference between stator core and rotor surface, based on the modified dual-salient permeance and the resultant improved MMF. Via the proposed model, a new analytical derivation featuring precise calculation of air-gap flux density is obtained to clarify the working mechanism of CPVPMM and give helpful design hints to fulfill high torque density. For the first time, it is identified the phenomenon of potential difference oscillation and additional harmonic exist in both CPVPMM and SVPMM. The influence of potential difference oscillation on working flux density is quantitatively analyzed, which reveals the operation principle of CPVPMM, and also unveils the underlying torque improvement mechanism over SVPMM, which gives new insight on enhancing torque of vernier machines. Finally, the analytical and FEA results are validated by experiments.**

***Index Terms*—Consequent pole, vernier PM machine, magnetic potential difference, torque density, simulation and analysis**

I. NOMENCLATURE

$\theta_{s,r}$	Position angle relative to stator and rotor, respectively
Ω	Mechanical angular velocity of rotor
$P_{r,s}$	Pole-pair number of rotor and armature winding, respectively
Z_s	Number of stator slots
$\tau_{s,r}$	Pole arc of stator and rotor, respectively
B_g	Open-circuit air-gap flux density
B_r	Amplitude of PM remanence flux density
F_{pm}	Magneto-motive force of PM array
F_m	Magnetizing magneto-motive force
$\Lambda_{s,r}$	Air-gap permeance of slotted stator and rotor, respectively
Λ_{sr}	Dual-salient air-gap permeance
$\lambda_{s,r}$	Relative permeance of slotted stator and rotor, respectively
$\lambda_{smin,rmin}$	Minimum value of relative air-gap permeance of slotted stator and rotor, respectively
Φ_{ri}	Flux through the i^{th} ferromagnetic pole
$\bar{\Lambda}_{ri}$	Lumped air-gap permeance above i^{th} ferromagnetic pole
$\varphi_{s,r}$	Magnetic potential of stator core and rotor core, respectively
φ_m	Magnetic potential of magnet surface
$\Delta\varphi$	Magnetic potential difference between stator core and rotor surface
$l_{s,r}$	Equivalent air-gap length of slotted stator and rotor, separately
r_g	Air-gap radius
l_{stk}	Axial stack length of machine
k_v	Winding factor of v^{th} harmonic
N_s	Turn number in series for one phase winding

II. INTRODUCTION

VERNIER permanent magnet machines (VPMM) have been extensively researched owing to their inherent high torque density, low torque ripple and simple structure [1-4], which cater to the surging need of low-speed, direct-drive applications from various industry sectors[2], [3].

Surface-mounted VPMM (SVPMM) were firstly proposed in [5], which generally have small armature pole pair P_s and large rotor pole pair P_r. The working principle of SVPMM i.e. flux modulation theory was proposed in [6] which reveals that by the teeth of open-slot stator, the P_s-pole-pair flux density is modulated to produce torque. Moreover, the torque produced by the modulated flux density will be amplified by pole ratio (PR) owing to "magnetic gearing effect", while PR is defined as the ratio of P_r to P_s. Therefore, the torque density of SVPMM is boosted to nearly twice that of the regular PM machine [7].

Based on the growing consensus of reducing heavy usage of rare-earth PM, consequent-pole (CP) magnet structure has gained increasing attention by replacing nearly half PMs with iron poles. With much reduced PM, considerably lower air-gap flux density, i.e. B_g in regular PM machines inevitably causes weaker torque capability than its surface-mounted counterparts [8]. Interestingly, when CP magnet rotor is applied in VPMM, the torque capability is even improved which is counterintuitive. In literature [9], consequent-pole VPMM (CPVPMM) with PR=11 is found to have higher torque density than SVPMM with even 40% reduced PM consumption. To reveal the torque improvement mechanism of CPVPMM over SVPMM, the accurate analytical investigation is highly required.

Numerous literatures are attributed to exploring the analytical modelling for VPMM. Typical approaches include the equivalent flux circuit method [10], sub-domain field method [11], conformal mapping method [12] and equivalent magnetomotive force (MMF)-permeance model [13].

This article has been accepted for publication in IEEE Transactions on Transportation Electrification. This is the author's version which has not been fully edited and content may change prior to final publication. Citation information: DOI 10.1109/TTE.2023.3301549

The first method calculates B_g by constructing typical lumped parameters along the flux path to reflect the flux distribution in the machine. However, the expression of B_g is quite complicated, while the result accuracy highly depends on the physical definition of the lumped parameters in the flux circuit. Sub-domain field method transforms the slotted air gap region into several sub-domain plains, B_g is calculated by solving the Laplace equation in the plain with simple boundary condition. Otherwise, this method cannot be directly applied in the machine with complex air gap structure and boundary conditions such as CPVPMM. Conformal mapping transforms the slotted domain into the slotless domains where B_g at any position can be obtained. However, iteration is required to solve the transformation between two domains for each point in the complete conformal point waveform. Besides, the accuracy of B_g would deteriorate as the slot opening width increase [14].

As for the equivalent MMF-permeance model, it has been mostly adopted in VPMM owing to its accurate and simple mathematical expression of B_g. By establishing MMF and permeance models based on the machine physical structure, B_g and machine sizing equation can be rapidly obtained. Moreover, the characteristics of B_g harmonics can be intuitively obtained thus revealing the machine working principle as well as the essential relationship between the local geometric parameters and the electromagnetic performance [5]-[12].

Currently, B_g in CPVPMM is usually calculated based on the equivalent MMF-permeance model as shown in Fig. 1.

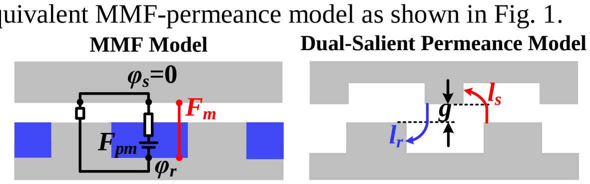

Fig. 1 The regular equivalent MMF-permeance model for CPVPMM.

The dual-salient air-gap permeance Λ_{sr} is usually simplified as (1-b) from (1-a) [15] by employing Λ_s and Λ_r, which is the single-salient permeance of slotted stator and rotor, respectively, and has definite harmonic expression [16].

$$\Lambda_{sr}(\theta_s,t)=\mu_0/\left(l_s(\theta_s)+l_r(\theta_s,t)-g\right) \tag{1-a}$$

$$\Lambda_{sr}(\theta_s,t)=g\Lambda_r(\theta_s,t)\Lambda_s(\theta_s)/\mu_0 \tag{1-b}$$

, where $l_{s,r}$ is the equivalent air-gap length of slotted stator and rotor, respectively. g is the air-gap length, μ_0 is the vacuum permeability. Λ_s and Λ_r is expressed as μ_0/l_s and μ_0/l_r, separately.

The equivalent MMF is the PM magnetizing MMF when stator is unslotted as expressed in (2) [15], where F_{pm} is the PM-excited MMF [17,18], φ_r is the magnetic potential of rotor core while that of stator core φ_s is assumed as 0.

$$F_m(\theta_s,t)=\varphi_r+F_{pm}(\theta_s,t) \tag{2}$$

It is noted that the conclusion of $\varphi_s=\varphi_r$ in regular PM machines cannot be applied to machine that adopts CP rotor due to the biased flux excitation of CP magnet, which should be offset by the additional potential difference between the stator and rotor core according to the Gauss Theorem.

In this paper, however, the analysis result of CPVPMM under different PR indicates that this regular modelling approach would cause deviated B_g and fundamental back EMF E_1. For one, the simplified Λ_{sr} is invalid in the dual-salient air gap, thus miscalculating the permeance harmonic contents. For another, MMF is different before and after stator is slotted.

What's more, the regular model would cause inaccurate analysis of the contribution to E_1 by individual B_g harmonic, which is the key to understand the operation essence of CPVPMM. Besides, the MMF-permeance model of SVPMM, which has single-salient air gap structure, is completely different from that of CPVPMM, thus it is difficult to directly compare and judge the factors that cause output torque advantage of CPVPMM over SVPMM.

In this paper, the modified Λ_{sr} and resultant improved MMF are derived by precisely defining two models. Further, a new analytical model $\Delta\varphi$ which is defined as the magnetic potential difference between the rotor surface and stator core, as shown in Fig. 2, is proposed for the first time. Via the proposed model, the E_1 generation mechanism of CPVPMM is accurately analyzed, while CPVPMM and SVPMM could be analyzed by the same analytical derivation (3) due to the same air-gap structure. Thus, the underlying torque improvement principle of CPVPMM over SVPMM can be quantitatively unveiled.

$$B_g(\theta_s,t)=\Delta\varphi(\theta_s,t)\Lambda_s(\theta_s) \tag{3}$$

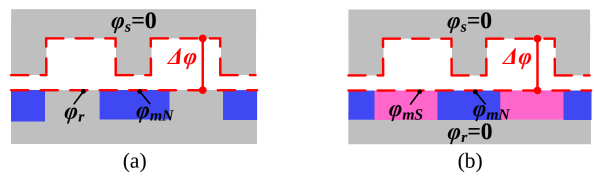

Fig. 2 Magnetic potential difference $\Delta\varphi$ model. (a) CPVPMM. (b) SVPMM.

The paper is organized as follows. In part III, the accurate MMF-permeance model for CPVPMM is analyzed. In part IV, the proposed model $\Delta\varphi$ in CPVPMM is analytically derived and is validated by FEA. The phenomenon of oscillating $\Delta\varphi$ and additional harmonics of $Z_s \pm P_r$ pole pairs, i.e. $\Delta\varphi_{Zs\pm Pr}$ is identified. In part V, a new analytical derivation of CPVPMM is obtained to analyze the electromagnetic performance. It turns out that $\Delta\varphi_{Zs\pm Pr}$ influences the amplitude of flux density, and is the key to accurately analyze the E_1 generation in CPVPMM. Then, the influences of structure parameters on E_1 is conducted via the $\Delta\varphi$ model, which decouples the interactive influence between rotor and stator dimensions unveiling the ideal major machine configurations. Further, the effect of iron saturation is taken into consideration to guide the appropriate design of structure parameters in regard of actual torque output under loaded condition. In part VI, CPVPMM and SVPMM are both analyzed via the oscillating $\Delta\varphi$ model. It is unveiled that the huge amplitude difference in $\Delta\varphi_{Zs\pm Pr}$ causes the torque advantage of CPVPMM over SVPMM. This result gives new insight on improving torque output of VPMM. Finally, a 12 slots/20 poles CPVPMM is manufactured based on the analysis result, and was tested to verify the analytical and FEA results.

III. Accurate Modelling of Equivalent Magneto-Motive Force and Air-Gap Permeance in CPVPMM

Fig.3 presents a typical CPVPMM, based on which the study is conducted. The PM magnetization direction is from the rotor to the stator, and the geometric parameters are given in Table I.

The following analysis is conducted on the assumptions:

This article has been accepted for publication in IEEE Transactions on Transportation Electrification. This is the author's version which has not been fully edited and content may change prior to final publication. Citation information: DOI 10.1109/TTE.2023.3301549

1). The permeability of ferrimagnet is assumed to be infinite.
2). B_g, MMF and Λ only vary in the circumference direction and is uniform in the radial and axial direction.

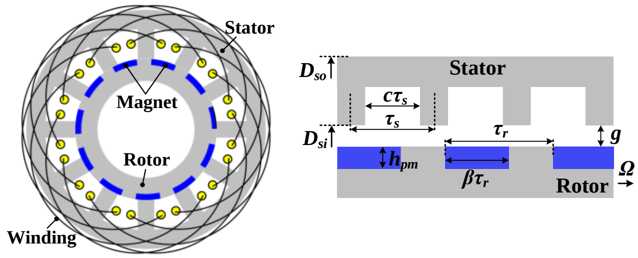

(a) (b)

Fig. 3 CPVPMM model (t=0).(a)Structure. (b)Detailed geometric parameters.

TABLE I
MAJOR STRUCTURE PARAMETERS OF CPVPMM

Parameters	value	Parameters	value
Stator outer radius, D_{so}	124mm	Air-gap length, g	0.7mm
Stator inner radius, D_{si}	74.4mm	Slot opening ratio, c	0.6
PM pole arc ratio, β	0.6	Stack length, L	70mm
Magnet thickness, h_{pm}	2.5mm	Rotating speed, Ω	300rpm
Stator slot number, Z_s	12	Rotor pole pair, P_r	11
Remanence flux density, B_r	1.235T(25℃)	Turn number in series per phase, N_s	400

A. Dual-salient Air-Gap Permeance in CPVPMM

Λ_{sr} is originally expressed as (1-a) which can be expressed as:

$$\Lambda_{sr}(\theta_s,t) = g\Lambda_r(\theta_s,t)\Lambda_s(\theta_s)k_\lambda/\mu_0\,,$$
$$k_\lambda = 1\big/\left(\lambda_r(\theta_s,t)+\lambda_s(\theta_s)-\lambda_r(\theta_s,t)\lambda_s(\theta_s)\right) \tag{4}$$

, where $\lambda_{s,r}$ is the relative permeance function of slotted stator and rotor, which equals to $g\Lambda_s/\mu_0$ and $g\Lambda_r/\mu_0$, respectively. Besides, k_λ is a λ_r and λ_s-related function.

k_λ has been widely approximated as 1 [16], thus (4) is usually simplified as (1-b). However, it is proved in this paper that "k_λ=1" is not valid in the whole dual-salient air gap region, and (1-a) would miscalculate the amplitude of major permeance harmonics, thus leading to the deviated prediction of B_g.

As shown in Fig.4, when the rotor iron pole is close to the stator tooth, $\lambda_{s,r}$ is close to 1, thus k_λ is nearly 1. However, when the magnet pole is moving towards the stator slot, $\lambda_{s,r}$ decreases towards 0 and k_λ considerably increases. At this time, Λ_{sr} will be much larger than that of (1-a). ***This means that B_g above magnet would be largely underrated if adopting simplified Λ_{sr}.***

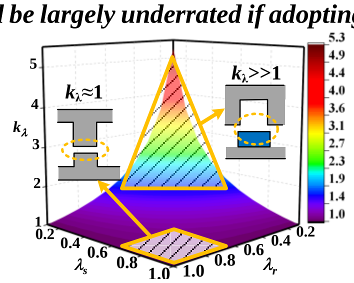

Fig. 4 Variation of k_λ along with different λ_s and λ_r.

The waveforms and harmonic spectra of original Λ_{sr} calculated by (4) and simplified Λ_{sr} calculated by (1-a) are compared to FEA result. As shown in Fig.5, the simplified Λ_{sr} would lead to large error in the amplitude of air-gap permeance harmonics, which in turn produces deviated prediction of B_g harmonics and their contribution to E_1. Thus, the original Λ_{sr} instead of simplified Λ_{sr} should be applied in CPVPMM.

It is noted that the FEA-simulated air-gap permeance is conducted on an equivalent electrostatic field-based method [19]. According to flux modulation theory, air-gap permeance Λ could be analytically calculated by (5), which means Λ equals to B_g if a simulation model is built which has the same air gap structure as the actual one, and a constant magnetic potential difference F=1A is added between the two sides of the air gap, as shown in Fig.6.

$$\Lambda(\theta) = B_g(\theta)/F(\theta) = B_g(\theta)\big|_{F(\theta)=1\mathrm{A}} \tag{5}$$

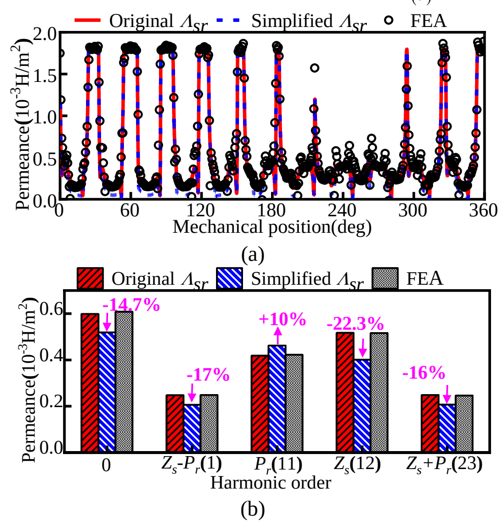

(a)

(b)

Fig. 5 Original Λ_{sr} calculated by (4) and simplified Λ_{sr} calculated by (1-b) and FEA results. (a) Waveforms. (b) Harmonic spectra.

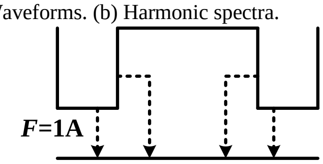

Fig. 6 Simulation model of air gap permeance.

However, the divergence of B_g is zero, which means the simulation model where B_g only distributes in the air gap cannot establish. Thus, an equivalent electrostatic field simulation model is adopted, where a constant potential difference of U=1V is excited between both sides of the air gap. According to the definition of electric field strength E, (6) is obtained, where $l_e(\theta)$ is the equivalent air-gap length at position θ.

$$l_e(\theta) = U(\theta)/E(\theta) = 1/E(\theta)\big|_{U(\theta)=1\mathrm{V}} \tag{6}$$

Combine (5) and (6), Λ could be calculated as (7) where E simulates the distribution path of flux lines. The simulated results via the proposed equivalent model have been validated by the analytical results which confirm its practicability [19].

$$\Lambda(\theta) = \mu_0 E(\theta)\big|_{U(\theta)=1\mathrm{V}} \tag{7}$$

B. Magnetizing Magneto-Motive Force in CPVPMM

As described in (2) in section II, $F_m(\theta_s, t)$is decided by φ_r and $F_{pm}(\theta_s, t)$ which can be expanded as (8) based on the CP rotor.

$$F_{pm}(\theta_s,t) \approx F_{pm0} + \sum_{n=1}^{3} F_{pmn}\sin(nP_r(\theta_s - \Omega t))$$
$$F_{pm0} = \beta B_r h_{pm}/(\mu_r\mu_0),\, F_{pmn} = 2B_r h_{pm}\sin(n\beta\pi)/(\mu_r\mu_0 n\pi) \tag{8}$$

, where F_{pm0} and F_{pmn} is the constant and n^{th} harmonic of F_{pm}, respectively. β is the PM pole arc ratio, B_r is the remanence flux density of magnet. h_{pm} is the magnet thickness, and μ_r is the relative permeability of magnet. It is noted that both even-order and odd-order MMF harmonic exist because of asymmetric magnetization of CP rotor structure.

Hence, the key of $F_m(\theta_s, t)$ lies in the accurate derivation of φ_r, which is found different before and after slotted.

Before stator is slotted, B_g could be calculated by (9), where Λ_r could be analytically expanded as (10).

$$B_g(\theta_s,t) = F_m(\theta_s,t)\Lambda_r(\theta_s,t) \tag{9}$$

$$\Lambda_r(\theta_s,t) = \Lambda_{r0} - \Lambda_{r1}\cos\left(P_r(\theta_s - \Omega t)\right) \tag{10}$$

, where Λ_{r0} and Λ_{r1} is the constant and fundamental permeance harmonic of slotted rotor, respectively [16].

According to Gauss theorem, B_g has no constant term and must satisfy (11). Then, φ_r could be derived by putting (8)-(10) into (11), which turns out to be (12).

$$\int_0^{2\pi} B_g(\theta_s,t)d\theta_s = 0 \tag{11}$$

$$\varphi_r = \frac{B_r h_{pm}}{\mu_r\mu_0}\left(\frac{\Lambda_{r1}\sin(\beta\pi)}{\pi\Lambda_{r0}} - \beta\right) \tag{12}$$

Based on (8)-(12), the waveform and harmonic spectra of B_g are given in Fig.7, where high agreements have been observed, validating the effectiveness of analytical model in (8)-(10).

After stator is slotted, B_g will be calculated by (13), where Λ_s could be analytically expanded as (14)

$$B_g(\theta_s,t) = F_m(\theta_s,t)\,g\Lambda_r(\theta_s,t)\Lambda_s(\theta_s)k_\lambda/\mu_0 \tag{13}$$

$$\Lambda_s(\theta_s) = \Lambda_{s0} + \Lambda_{s1}\cos\left(Z_s\theta_s\right) \tag{14}$$

, where Λ_{s0} and Λ_{s1} is the constant and fundamental permeance harmonic of slotted stator, respectively [16].

It is also noted that k_λ has λ_r and λ_s in denominator, which makes it hard to analyze. Herein, k_λ is simplified as (15), where λ_{rmin} is the minimum value of λ_r. The detailed derivation procedure of k_λ is given in the appendix.

$$k_\lambda \approx \left[(1-\lambda_r)\lambda_{r\min}\left(k_1\lambda_s^2 + k_2\lambda_s + k_3\right) + \left(\lambda_r - \lambda_{r\min}\right)\right]\Big/(1-\lambda_{r\min}) \tag{15}$$

By putting (8)-(11) and (13)-(15) into (12), φ_r is then obtained as (16), where coefficient A_1-A_4 are given in appendix. It is found that φ_r is related to Λ_{s0} and Λ_{s1}, which indicates that the stator slotting will have effect on φ_r and $F_m(\theta_s, t)$.

$$\varphi_r = -\frac{2B_r h_{pm}\sin(\beta\pi)}{\mu_r\mu_0\pi}\frac{A_1\Lambda_{s0} + A_2\Lambda_{s1}}{A_3\Lambda_{s0} + A_4\Lambda_{s1}/2} - \frac{\beta B_r h_{pm}}{\mu_r\mu_0} \tag{16}$$

Further, the waveforms of equivalent $F_m(\theta_s, t)$ under both unslotted and slotted stator are plotted in Fig.8. It proves that φ_r and $F_m(\theta_s, t)$ are different before and after stator is slotted. However, when the simplified Λ_{sr} is adopted in the above analysis, the analytical result of φ_r turns out to be the same as (12) regardless of stator slotting.

This indicates that via the simplified Λ_{sr} model, the inaccurate $F_m(\theta_s, t)$ would lead to deviated B_g of CPVPMM. Finally, the accurate expression of $F_m(\theta_s, t)$ is given in (17), which is actually highly related to the stator slotting effect.

$$\begin{aligned} F_m(\theta_s,t) &= \varphi_r + F_{pm}(\theta_s,t) = F_0 + \sum_{n=1}^{3} F_{pmn}\sin(nP_r(\theta_s - \Omega t)) \\ F_0 &= -\frac{2B_r h_{pm}\sin(\beta\pi)}{\mu_r\mu_0\pi}\frac{A_1\Lambda_{s0} + A_2\Lambda_{s1}}{A_3\Lambda_{s0} + A_4\Lambda_{s1}/2} \end{aligned} \tag{17}$$

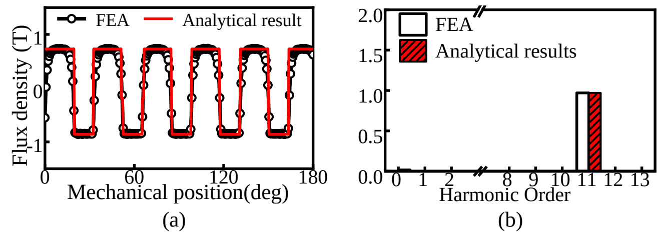

Fig. 7 B_g of unslotted CPVPMM calculated via analytical and FEA method. (a) Waveforms. (b) Harmonic spectra.

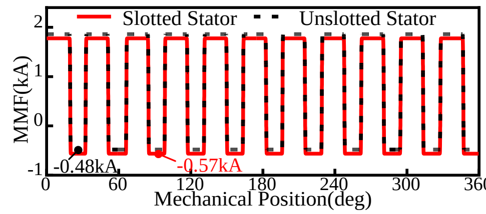

Fig. 8 Waveform of $F_m(\theta_s,t)$ of unslotted CPVPMM and slotted CPVPMM.

IV. Magnetic Potential Difference Between Stator Core and Rotor Surface in CPVPMM

A. Magnetic Potential Difference Model

Based on the accurate modelling Λ_{sr} and $F_m(\theta_s, t)$ as presented in section III, B_g could be obtained as shown in (18) to facilitate machine analysis and design. However, both F_m and Λ_{sr} are Λ_r and Λ_s-related fractions, which not only makes it impossible to establish the concise analytical expression of working flux density, but also tangles the influence of stator and rotor structural parameters on machine performance.

$$\begin{aligned} B_g(\theta_s,t) &= F_m(\theta_s,t)\Lambda_{sr}(\theta_s,t) \\ &= \left[F_0 + \sum_{n=1}^{3} F_{pmn}\sin(nP_r(\theta_s - \Omega t))\right] \times \left\{\begin{aligned} &\frac{gk_\lambda}{\mu_0}\left[\Lambda_{s0} + \Lambda_{s1}\cos\left(Z_s\theta_s\right)\right] \\ &\times\left[\Lambda_{r0} - \Lambda_{r1}\cos\left(P_r(\theta_s - \Omega t)\right)\right] \end{aligned}\right\} \end{aligned} \tag{18}$$

To solve this issue, a new analytical model, the magnetic potential difference between stator core and rotor surface i.e. $\Delta\varphi$, is proposed as illustrated in Fig.2. Accordingly, a new analytical approach i.e. $\Delta\varphi$-Λ_s model is derived to analyze B_g, where $\Delta\varphi$ takes the rotor salience into account thus decoupling the electromagnetic influence between stator and rotor.

Because B_g could be expressed by both (3) and (13), $\Delta\varphi$ of CPVPMM could be obtained by simultaneous equation (19).

$$\begin{aligned} F_m(\theta_s,t)\,g\Lambda_r(\theta_s,t)\Lambda_s(\theta_s)k_\lambda/\mu_0 &= \Delta\varphi(\theta_s,t)\Lambda_s(\theta_s) \\ \Delta\varphi(\theta_s,t) &= F_m(\theta_s,t)\lambda_r(\theta_s,t)k_\lambda \end{aligned} \tag{19}$$

Then, $\Delta\varphi$ can be calculated as (20).

$$\begin{aligned} \Delta\varphi(\theta_s,t) = {} & \Delta\varphi_0 + \Delta\varphi_{Z_s}\sin(Z_s\theta_s) + \Delta\varphi_{P_r}\sin(P_r\theta_s - P_r\Omega t) \\ & + \Delta\varphi_{Z_s\pm P_r}\sin((Z_s \pm P_r)\theta_s \mp P_r\Omega t) \end{aligned}$$

$$\begin{cases} \Delta\varphi_0 = (2F_0A_3 + A_1F_{pm1})/2 \\ \Delta\varphi_{P_r} = (2F_0A_1 + (A_3 - A_5)F_{pm1} + A_5F_{pm3})/2 \\ \Delta\varphi_{Z_s} = F_0A_4 + A_2F_{pm1} \\ \Delta\varphi_{Z_s\pm P_r} = (2F_0A_2 + (A_4 - A_6)F_{pm1} + A_6F_{pm3})/2 \end{cases} \tag{20}$$

, where $\Delta\varphi_0$ and $\Delta\varphi_n$ is the constant and n^{th} harmonic of $\Delta\varphi$, respectively, while other harmonics are not expounded herein. Coefficient A_5, A_6 are also presented in the appendix.

This article has been accepted for publication in IEEE Transactions on Transportation Electrification. This is the author's version which has not been fully edited and content may change prior to final publication. Citation information: DOI 10.1109/TTE.2023.3301549

From (20), it is revealed that $\Delta\varphi$ oscillates when rotor rotates, thus additional harmonic $\Delta\varphi_{Zs\text{-}Pr}$ and $\Delta\varphi_{Zs+Pr}$ exist apart from the fundamental harmonic $\Delta\varphi_{Pr}$. Besides, $\Delta\varphi_{Zs\text{-}Pr}$ and $\Delta\varphi_{Zs+Pr}$ rotates at fundamental electrical angular speed in the anticlockwise direction and clockwise direction, respectively.

B. The Phenomenon of Oscillating Magnetic Potential Difference

The waveforms of $\Delta\varphi(\theta_s, t)$ at t=0 and t_1, e.g. $t_1=2\pi/(5P_r\Omega)$, calculated by (21) are then compared to the result which is calculated by $B_g(\theta_s, t)/\Lambda_s(\theta_s)$, B_g and Λ_s are both FEA-predicted.

As shown in Fig.9 (a), high agreement between two methods proves the accuracy of the proposed analytical approach. It is proved that the amplitude of $\Delta\varphi$ oscillates as rotor rotates, i.e. the valley of waveform moves anticlockwise by 2π/5.

It implies that additional time-space $\Delta\varphi$ harmonics exist, and one of them is rotating anticlockwise at speed of $P_r\Omega$, which accords with $\Delta\varphi_{Zs\text{-}Pr}$ in (20). Further, the harmonic spectra of oscillating $\Delta\varphi$ is presented in Fig.9(b), $\Delta\varphi_{Zs\pm Pr}$ is negative which means it has the opposite initial phase to that of $\Delta\varphi_{Pr}$.

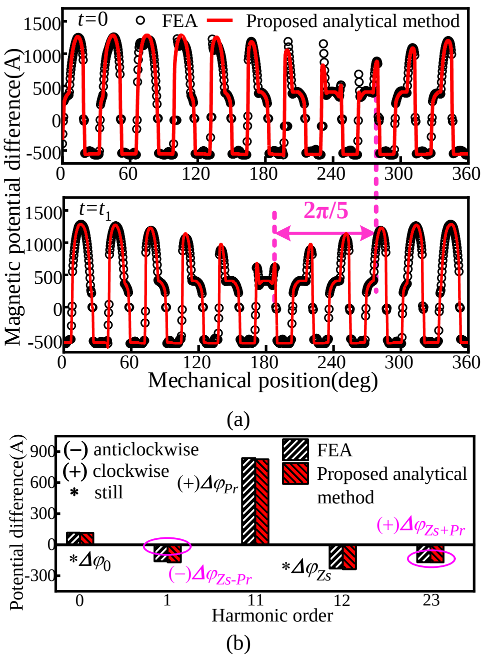

Fig. 9 $\Delta\varphi$ in CPVPMM calculated by the proposed analytical method and FEA. (a) Waveforms at t=0 and t_1. (b) Harmonic spectra.

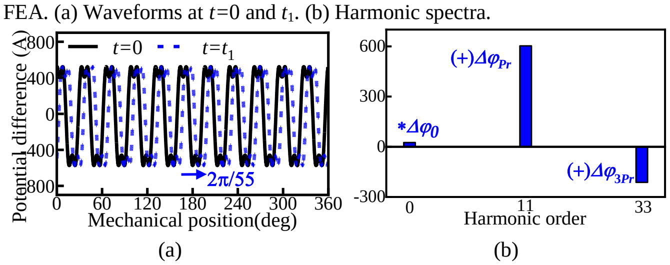

Fig. 10 $\Delta\varphi$ in CPVPMM at t=0 and t=t_1 calculated by the regular analytical method. (a) Waveforms at t=0 and t_1. (b) Harmonic spectra.

However, when the regular analytical model with simplified Λ_{sr} and $F_m(\theta_s,t)$ is adopted in analyzing $\Delta\varphi$, $\Delta\varphi$ will be calculated as (21), where $\Delta\varphi$ is merely decided by $F_m(\theta_s,t)$ and $\lambda_r(\theta_s,t)$. In this situation, the waveforms and harmonic spectra of $\Delta\varphi$ at t=0 and t_1 are plotted in Fig.10. It shows that the amplitude of $\Delta\varphi_{Pr}$ is 28% smaller than FEA result. Moreover, the amplitude of $\Delta\varphi$ remains constant as rotor rotates thus only $\Delta\varphi_{nPr}$ (n is integer) exist, the additional harmonics $\Delta\varphi_{Zs\pm Pr}$ will not exist, which opposes to the FEA result in Fig. 9.

$$\Delta\varphi(\theta_r)=F_m(\theta_s,t)\lambda_r(\theta_s,t)=\sum_{n=0,1,2,3}\Delta'\varphi_{nP_r}\cos(nP_r(\theta_s-\Omega t))$$
$$\Delta'\varphi_0=(2F_0\lambda_{r0}-F_{pm1}\lambda_{r1})/2,\quad \Delta'\varphi_{P_r}=F_{pm1}\lambda_{r0}-F_0\lambda_{r1} \qquad (21)$$
$$\Delta'\varphi_{2P_r}=(F_{pm1}\lambda_{r1})/2,\quad \Delta'\varphi_{3P_r}=(2F_{pm3}\lambda_{r0}-F_{pm2}\lambda_{r1})/2$$

Hence, the simplified Λ_{sr} not only causes the smaller $\Delta\varphi_{Pr}$, but also omits the crucial phenomenon of oscillating $\Delta\varphi$ and additional harmonics $\Delta\varphi_{Zs\pm Pr}$, which is the key to understand the working mechanism of CPVPMM as will analyzed after.

V. Study of CPVPMM Based on Magnetic Potential Difference Model

A. Analytical Sizing Equation of CPVPMM

B_g calculated via the oscillating $\Delta\varphi$ model can be expressed as (22-a), while B_g calculated via the non-oscillating $\Delta\varphi$ model is expressed as (22-b). The waveforms and harmonic spectra of B_g acquired by (22) are compared to the FEA result. As shown in Fig.11, B_g calculated by the oscillating $\Delta\varphi$ model agrees well with FEA result. However, via the non-oscillating $\Delta\varphi$ model, $B_{Zs\pm Pr}$ is 12% larger and B_{Pr} is 23% smaller than the FEA result. ***Especially, B_g above magnet is considerably underrated when adopting simplified Λ_{sr}, which validates the above analysis.***

$$\begin{aligned}B_g&=(\Delta\varphi_0\Lambda_{s0}+0.5\Delta\varphi_{Z_s}\Lambda_{s1})+\Delta\varphi_{Z_s}\Lambda_{s0}\sin(Z_s\theta_s)\\&+\left[\Delta\varphi_{P_r}\Lambda_{s0}+\frac{\Delta\varphi_{Z_s-P_r}+\Delta\varphi_{Z_s+P_r}}{2}\Lambda_{s1}\right]\sin\left(P_r\theta_s-P_r\Omega t\right)\\&+(0.5\Delta\varphi_{P_r}\Lambda_{s1}+\Delta\varphi_{Z_s\pm P_r}\Lambda_{s0})\sin\left((Z_s\pm P_r)\theta_s\mp P_r\Omega t\right)\end{aligned} \qquad (22\text{-a})$$

$$\begin{aligned}B_g&=0.5\Delta\varphi_0\Lambda_{s0}+\Delta\varphi_{P_r}\Lambda_{s0}\sin\left(P_r(\theta_s-\Omega t)\right)\\&+0.5\Delta\varphi_{P_r}\Lambda_{s1}\sin\left((Z_s\pm P_r)\theta_s\mp P_r\Omega t\right)\end{aligned} \qquad (22\text{-b})$$

To figure out, the generation of B_{Pr} and $B_{Zs\pm Pr}$ by $\Delta\varphi$ harmonic from two $\Delta\varphi$ models are given in Fig.12. Via the oscillating $\Delta\varphi$ model, it turns out that $\Delta\varphi_{Zs\pm Pr}$ undermines both B_{Pr} and $B_{Zs\pm Pr}$. However, via the non-oscillating $\Delta\varphi$ model, B_{Pr} and $B_{Zs\pm Pr}$ are only created by $\Delta\varphi_{Pr}$ which is underestimated. As a result, the inaccurate $\Delta\varphi_{Pr}$ and absence of $\Delta\varphi_{Zs\pm Pr}$ in the regular analytical method underestimate B_{Pr} while overestimate $B_{Zs\pm Pr}$.

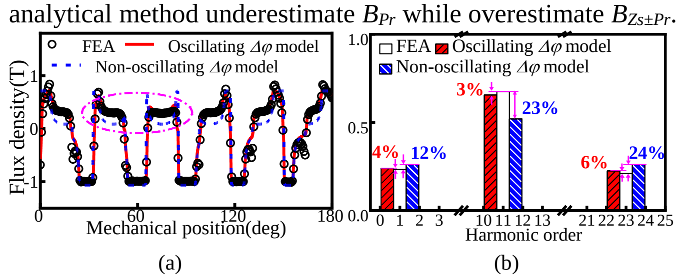

Fig. 11 B_g of unslotted CPVPMM calculated via analytical and FEA method. (a) Waveforms. (b) Harmonic spectra.

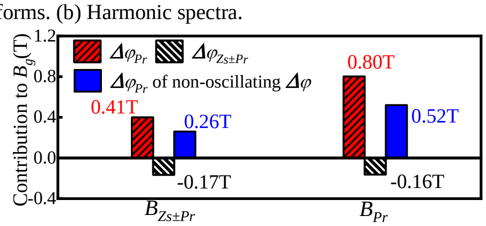

Fig. 12 Waveform of $F_e(\theta_s,t)$ of unslotted CPVPMM and slotted CPVPMM.

This article has been accepted for publication in IEEE Transactions on Transportation Electrification. This is the author's version which has not been fully edited and content may change prior to final publication. Citation information: DOI 10.1109/TTE.2023.3301549

Further, the phase back EMF E_n, and the amplitude of fundamental back EMF E_1 can be calculated by (23).

$$\begin{aligned} E_n(t) &= -\frac{d}{dt} r_g l_{stk} \int_0^{2\pi} B_g(\theta_s,t) N_{wn}(\theta_s) d\theta_s \\ E_1 &= 2 r_g l_{stk} N_s P_r \Omega \left[B_{P_r} k_{wP_r} / P_r + B_{Z_s \pm P_r} k_{wZ_s \pm P_r} / (Z_s \pm P_r) \right] \end{aligned} \tag{23}$$

, where r_g is the air-gap radius, l_{stk} is the stack length, N_{wn} is the phase n winding function, k_{wv} is the winding factor of v^{th} armature harmonic, N_s is the serial turn number per phase. B_v is the amplitude of v^{th} flux density.

According to the electromechanical conversion principle, the average torque T of CPVPMM could be generated as (24).

$$T = (E_a i_a + E_b i_b + E_c i_c)/\Omega = 3E_1 I_m/2 \tag{24}$$

, where I_m is the amplitude of phase current. It is noted that i_d=0 control is usually adopted because L_q/L_d nearly equals to 1, which is caused by the rotor anisotropic feature in VPMM [20].

It is found that T can be reflected by E_1 when saturation in iron core is ignored. In this means, E_1 and the E_1 contribution by individual flux density harmonic is of vital importance.

In Fig.13, the E_a waveforms and harmonic spectra calculated by the oscillating $\Delta\varphi$ model and non-oscillating $\Delta\varphi$ model are compared to FEA result. The result calculated by the oscillating $\Delta\varphi$ model agrees well with that of FEA, while E_1 calculated by the non-oscillating $\Delta\varphi$ model deviates from FEA result by 6.5%.

The deviation seems smaller than that of flux density in Fig.11. It can be explained via the contribution to E_1 by B_{Pr} and $B_{Zs\pm Pr}$ based on (23), as plotted in Fig.14 (a). It shows that $B_{Zs\pm Pr}$ is the major contributor owing to amplifying effect of PR, especially when PR is high. Thus, the large discrepancy in B_{Pr} slightly reduces E_1 and can be made up by that induced by $B_{Zs\pm Pr}$, which makes the deviation in total E_1 not quite large.

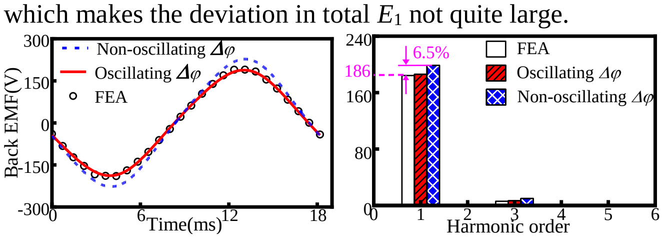

(a) (b)

Fig. 13 Back EMF of CPVPMM by FEA and two $\Delta\varphi$ models. (a) Waveforms. (b) Harmonic spectra.

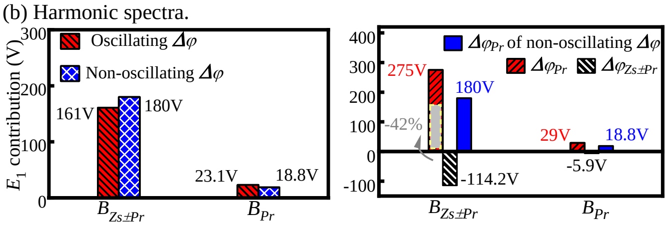

(a) (b)

Fig. 14 Contribution to E_1 by B_{Pr} and $B_{Zs\pm Pr}$. (a) Results via two $\Delta\varphi$ models. (b) B_{Pr} and $B_{Zs\pm Pr}$ are decomposed into components created by $\Delta\varphi$ harmonics.

Further, B_{Pr} and $B_{Zs\pm Pr}$ are decomposed into the component created by $\Delta\varphi$ harmonic as shown in Fig.14(b). Via the oscillating $\Delta\varphi$ model, E_1 induced by the individual flux density has two components, the positive part derives from $\Delta\varphi_{Pr}$ while negative part derives from $\Delta\varphi_{Zs\pm Pr}$. As for E_1 induced by $B_{Zs\pm Pr}$, the negative part offsets 42% of the positive one. However, via the non-oscillating $\Delta\varphi$ model, E_1 induced by B_{Pr} and $B_{Zs\pm Pr}$ has only one component.

In the next part, CPVPMM with different PR will be analyzed to illustrate the important effect of oscillating $\Delta\varphi$ on the specific E_1 contribution of B_{Pr} and $B_{Zs\pm Pr}$, as well as the accurate prediction of E_1 in the whole range of PR.

B. Generation of back EMF in CPVPMM of Different PR

Five CPVPMM with different PR in Fig.15 are studied, of which the major structural parameters are presented in Table. II. Five machines have the same size, the same magnet thickness and pole arc, and the same stator slot opening ratio, except for the number of rotor pole pairs. PR of five machines is 5/7, 7/5, 2, 5 and 11 while the corresponding slot/pole combination is 12/10, 12/14, 12/16, 12/20 and 12/22, respectively.

Then, the E_1 of five machines calculated by the oscillating $\Delta\varphi$ model, non-oscillating $\Delta\varphi$ model and FEA are compared in Fig.16. It shows that the difference between E_1 calculated via the oscillating $\Delta\varphi$ model and FEA in five models are all smaller than 2%. However, the error between E_1 calculated via the non-oscillating $\Delta\varphi$ model and FEA results increases as PR grows, the error is -16% when PR is 5/7, and gradually increases to almost 0 when PR is 5, then it reaches 6% when PR is 11.

This means in CPVPMM of certain PR, E_1 predicted via the non-oscillating $\Delta\varphi$ model might be close to the FEA result. However, the apparent error exists in the whole PR range due to the wrong prediction of B_{Pr} and $B_{Zs\pm Pr}$ thus leading to the misinterpreted E_1 composition.

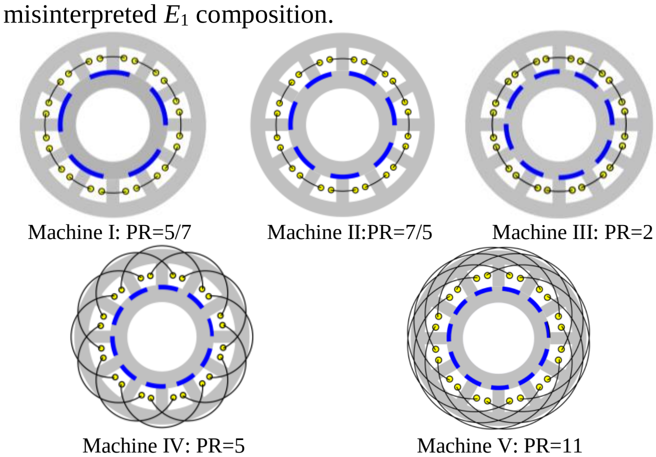

Fig. 15 Five CPVPMM models with different PR.

TABLE II
MAJOR MACHINE PARAMETERS OF FIVE CPVPMMS

Parameters	Machine I	Machine II	Machine III	Machine IV	Machine V
Stator slot number			12		
Rotor pole pairs	5	7	8	10	11
Coil pitch	1	1	1	3	6
Winding factor	0.97	0.97	0.87	1	1
Stator outer diameter			124mm		
Stator inner diameter			74.4mm		
Stack length			70mm		
Air-gap length			0.7mm		
Stator slot open ratio			0.6		
Magnet thickness			2.5mm		
PM Pole arc ratio			0.6		
Magnet trademark			N38UH		
Silicon steel trademark			35TW250		
Remanence flux density			1.235T(20°C)		

This article has been accepted for publication in IEEE Transactions on Transportation Electrification. This is the author's version which has not been fully edited and content may change prior to final publication. Citation information: DOI 10.1109/TTE.2023.3301549

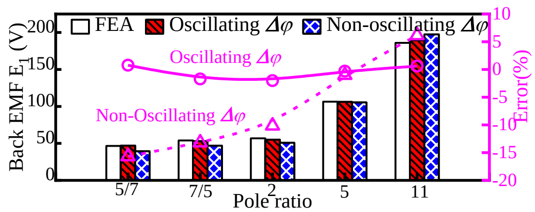

Fig. 16 E_1 calculated via the oscillating $\Delta\varphi$ model and non-oscillating $\Delta\varphi$ model and FEA.

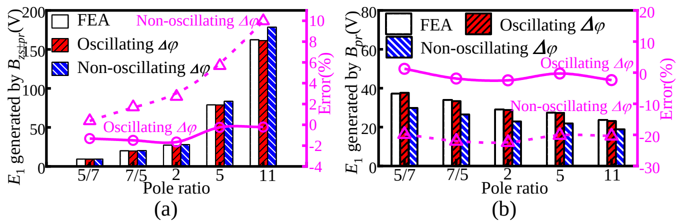

Fig. 17 E_1 generated by B_{Pr} and $B_{Zs\pm Pr}$ via FEA and two $\Delta\varphi$ models. (a) E_1 contributed by $B_{Zs\pm Pr}$. (b) E_1 contributed by B_{Pr}

The generation of E_1 by B_{Pr} and $B_{Zs\pm Pr}$ calculated via two $\Delta\varphi$ models are also compared to the FEA results in Fig.17. It shows that the discrepancy between E_1 created by $B_{Zs\pm Pr}$ and FEA result is surging as PR increases because $B_{Zs\pm Pr}$ is overrated by the non-oscillating $\Delta\varphi$ model. Meanwhile, the error between the E_1 generated by B_{Pr} and the FEA result is about -20% due to the underrated B_{Pr}. However, the error between the results from oscillating $\Delta\varphi$ model and FEA is smaller than 5%.

Hence, with the assistance of the oscillating $\Delta\varphi$ model, the E_1 generation of CPVPMM can be accurately interpreted.

C. *Design Principle*

Based on the proposed oscillating $\Delta\varphi$ model, the dual-salient air gap in CPVPMM is converted into single-salient, i.e. stator-slotted air gap. Hence, the flux density is calculated by the according $\Delta\varphi$-Λ_s model, where $\Delta\varphi$ is only decided by the rotor structure, while Λ_s derives from the stator structure. In this means, the interaction between F_m and Λ_{sr} is decoupled by putting the effect of Λ_r into $\Delta\varphi$, then the influences of rotor/stator structure parameters could be separately studied.

In this part, the effects of magnet pole arc ratio β, magnet thickness h_{pm}, and stator slot open ratio c, are studied in regard of B_{Pr} and $B_{Zs\pm Pr}$. Moreover, the effect of saturation in rotor iron pole on the machine performance is also analyzed, which helps to design the optimal structure parameters so as to satisfy the output torque. The findings in this study will provide useful hints when designing high-torque density CPVPMM. Take 12slots/22poles CPVPMM in Table I to illustrate.

1) *Effect of Rotor Structure*

The variation of $\Delta\varphi_{Pr}$ and $\Delta\varphi_{Zs\pm Pr}$ along with a series of h_{pm} under different β is plotted and shown in Fig.18. It shows that as h_m increases, both $\Delta\varphi_{Pr}$ and $\Delta\varphi_{Zs\pm Pr}$ increase. Moreover, $\Delta\varphi_{Pr}$ has much wider varying range than $\Delta\varphi_{Zs\pm Pr}$ in the overall h_{pm} range. Further, the variation of $\Delta\varphi_{Pr}$ and $\Delta\varphi_{Zs\pm Pr}$ along with a series of β under different h_{pm} is studied and presented in Fig.19.

It shows that as β increases, $\Delta\varphi_{Zs\pm Pr}$ increases to the maximum where β is around 0.6 and then decreases. However, $\Delta\varphi_{Pr}$ under different h_{pm} shows different trend, i.e. when h_{pm} is below 3.5mm, it has similar trend as $\Delta\varphi_{Zs\pm Pr}$; when h_{pm} is larger than 3.5mm, $\Delta\varphi_{Pr}$ is gradually increasing as h_{pm} increases. This phenomenon indicates that as h_{pm} increases, the impact of negative $\Delta\varphi_{Zs\pm Pr}$ could be better restrained by the positive $\Delta\varphi_{Pr}$ so that working flux density would have larger amplitude.

It is indicated that the optimal β in CPVPMM is around 0.6. Moreover, thick magnet is suitable for CPVPMM. This is an important conclusion because thick magnet cannot be adopted in SVPMM due to reduced flux modulation effect [3].

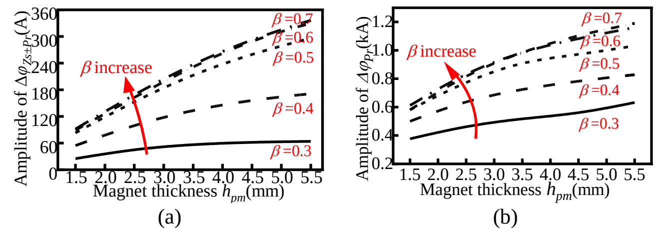

Fig. 18 Influence of magnet thickness on $\Delta\varphi$ harmonics. (a) $\Delta\varphi_{Pr}$ (b) $\Delta\varphi_{Zs\pm Pr}$

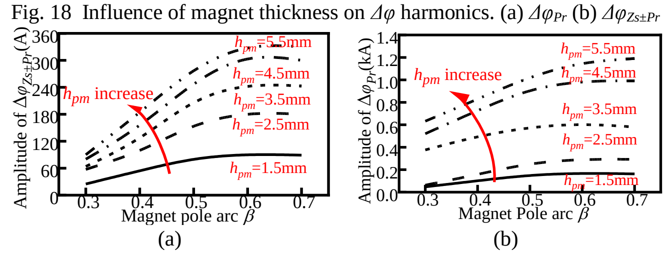

Fig. 19 Influence of magnet pole arc ratio on $\Delta\varphi$ harmonics. (a) $\Delta\varphi_{Pr}$ (b) $\Delta\varphi_{Zs\pm Pr}$.

2) *Effect of Stator Structure*

Via the oscillating $\Delta\varphi$ model, it is known that the stator slot open ratio c would impact Λ_{sr} which in return influences $\Delta\varphi$. Thus, the influence of c on $\Delta\varphi$ should be studied at first. When β is designed as 0.6 and h_{pm} is 2.5mm, the variation of $\Delta\varphi_{Pr}$ and $\Delta\varphi_{Zs\pm Pr}$ along with a series of c is studied and presented in Fig.20 (a). It is revealed that $\Delta\varphi_{Pr}$ keeps increasing when c increases while $\Delta\varphi_{Zs\pm Pr}$ climbs to the maximum at c=0.7 and begins to fall. Besides, the influence of c on Λ_{s0} and Λ_{s1} is also studied and presented in Fig. 20 (b). It shows that Λ_{s0} keeps decreasing as c increases which is opposed to that of $\Delta\varphi_{Pr}$, but Λ_{s1} exhibits the similar trend as that of $\Delta\varphi_{Zs\pm Pr}$, that is Λ_{s1} first increasing to the top at c=0.6 before starting to decrease.

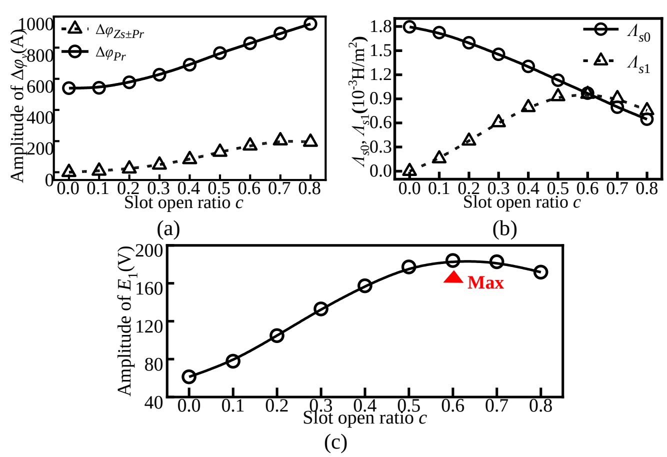

Fig. 20 Influence of stator slot open ratio c. (a) Amplitude of $\Delta\varphi$ harmonics. (b) Amplitude of Λ_s harmonics. (c) Amplitude of E_1.

According to (27), the effect of c on E_1 can be reflected by combining the effect of c on $\Delta\varphi$ and Λ_s, as shown in Fig. 20(c). It shows that E_1 has the similar trend as that of Λ_{s1}: E_1 increases to the maximum when c equals to 0.6 before decreasing. It is

This article has been accepted for publication in IEEE Transactions on Transportation Electrification. This is the author's version which has not been fully edited and content may change prior to final publication. Citation information: DOI 10.1109/TTE.2023.3301549

analyzed that the strengthening effect of $\Delta\varphi_{Pr}$ is neutralized by the mitigating effect of Λ_{s0}, while the amplitude variation of $\Delta\varphi_{Zs\pm Pr}$ is quite limited. ***Hence, the influence of c on E_1 is basically decided by Λ_{s1}, and the optimal c is around 0.6.***

3) *Effect of Saturation in Rotor Iron Pole*

Similar to the regular MMF-permeance model, the proposed $\Delta\varphi$ model is carried out based on the assumption of ignoring iron core saturation. In this sector, the effect of core saturation on the accuracy of the proposed analytical model as well as the actual torque output will be studied with the assistance of FEA.

The flux density contours of CPVPMM model under different electric loading A are plotted in Fig. 21, where the major saturation actually happens in the rotor iron pole and gets severer as A increases due to stronger armature reaction [18].

Then, the effect of different iron pole saturation on air gap flux density established by PM is studied by frozen permeability (FP) method [21], as shown in Fig. 22. It shows that the amplitude of working harmonics slightly decreases as saturation gets severer, while the phase angle of B_{Pr} merely changes. However, the phase of $B_{Zs\text{-}Pr}$ varies as A increases because Λ_r is altered by iron pole saturation, indicating the amplitude and phase of E_1 both change as A increases.

To clarify, the contribution of E_1 by B_{Pr} and $B_{Zs\text{-}Pr}$ and total E_1 under different A are calculated and presented in Table III which has been validated by FEA (FP).

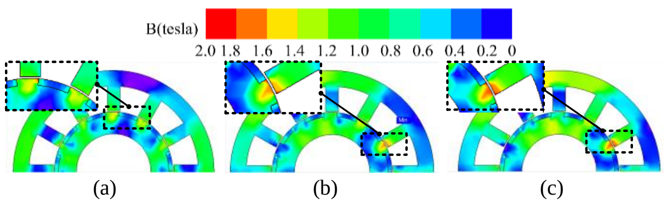

Fig. 21 Saturation of rotor iron pole under different electric loading A. (a) A=0A/cm. (b) A=100A/cm. (c) A=150A/cm.

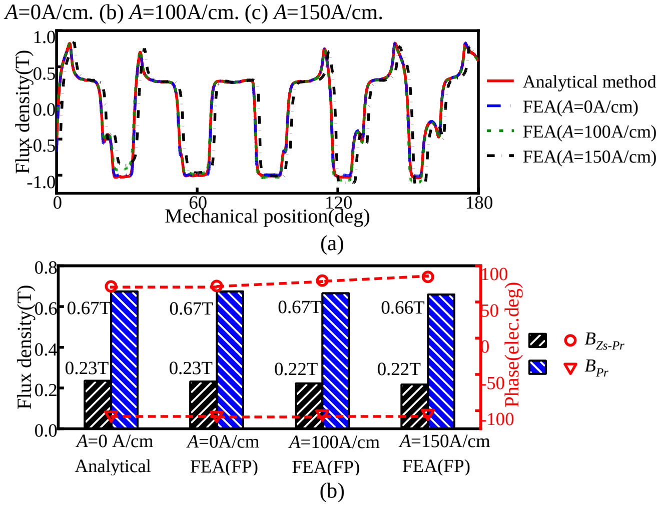

Fig. 22 B_g (t=0s) established by magnet under different electric loading A. (a) Waveforms. (b) Harmonic spectra.

TABLE III
BACK EMF E_1 CONTRIBUTION BY $B_{Zs\text{-}Pr}$ AND B_{Pr} UNDER DIFFERENT A

E_1 contribution	A=0 A/cm		A=100 A/cm		A=150 A/cm	
	$B_{Zs\text{-}Pr}$	B_{Pr}	$B_{Zs\text{-}Pr}$	B_{Pr}	$B_{Zs\text{-}Pr}$	B_{Pr}
Amplitude(V)	165	19	161	18.7	158	18.5
Phase(elec. deg)	108.5	106.2	100.5	104.4	95.4	103.6
Total E_1	184∠108°		179.6∠101°		176∠96°	

It is found that the amplitude of total E_1 decreases by 4%, while the phase angle deviates by 11%, ***indicating that the phase current angle should be adjusted according to actual E_1 angle instead of open-circuit one so as to output larger average torque.***

Further, the characteristics of actual torque along with magnet pole arc ratio β are studied by FEA and compared to analytical results, as presented in Fig. 23. It is shown the torque variations from two methods have the similar characteristic that is the maximum torque is obtained when β is about 0.6, which also accords with the analytical result in *1)*.

Hence, the rotor iron pole saturation does not affect the flux density composition and E_1 generation despite reducing amplitude. Therefore, the proposed analytical method is always feasible for the analysis and design of CPVPMM.

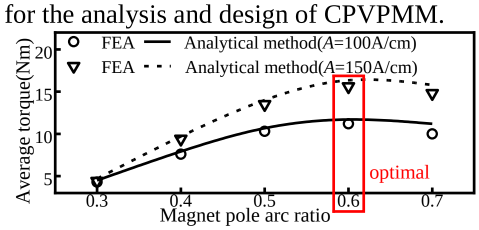

Fig. 23 Average torque variation with magnet pole arc under different A.

VI. Comparison Study of CPVPMM And SVPMM Based on Oscillating Potential Difference Model

Due to the facts that air gap length and permeance components in CPVPMM and SVPMM are different, the MMF-permeance models of two machines are completely different which makes it tricky to figure out the reasons that cause the torque advantage of CPVPMM over SVPMM.

Owing to the proposed $\Delta\varphi$ model, the air-gap structure of CPVPMM transforms into the same stator-slotted one as that of SVPMM, ***which unifies the length of air gap while the comparison between CPVPMM and SVPMM only lies in $\Delta\varphi$***.

In the following analysis, SVPMM that has the same major sizes in Table. I except that β=0.5 is taken for example.

A. *Open-Circuit Back EMF*

To begin with, $\Delta\varphi$ of SVPMM is obtained when the equivalent air-gap length g' is taken into by MMF so that air-gap permeance in SVPMM is also decided by the physical air-gap length g. $\Delta\varphi$ of SVPMM is then calculated by (25) and Fourier expressed as (26), where $\Delta\varphi_{Zs\pm Pr}$ exist implying that $\Delta\varphi$ of SVPMM also oscillates.

$$\Delta\varphi(\theta_s, t) = F_e \Lambda_s^{'} / \Lambda_s \tag{25}$$

, where Λ'_s is the stator-slotted permeance function when the equivalent air-gap length g' is $g+h_{pm}/\mu_r$.

The waveforms of $\Delta\varphi$ (t=0s) are obtained by (26) and compared to FEA result. As shown in Fig. 24, high agreement is observed which validates (26). Then, the harmonic spectra of $\Delta\varphi$ in CPVPMM and SVPMM are compared in Fig. 25, where $\Delta\varphi_{Zs\pm Pr}$ in SVPMM is negative, so it also reduces working flux density. ***Moreover, $\Delta\varphi_{Zs\pm Pr}$ in SVPMM triples that of CPVPMM, while $\Delta\varphi_{Pr}$ only enhances by 51%.*** Then, the influence of different $\Delta\varphi_{Zs\pm Pr}$ and $\Delta\varphi_{Pr}$ content between CPVPMM and SVPMM is analyzed in regard of electromagnetic performance.

$$\Delta\varphi(\theta_s,t)=\sum_{n=1,3,5}\Delta\varphi_{nP_r}\sin\left[nP_r(\theta_s-\Omega t)\right]+\Delta\varphi_{Z_s\pm P_r}\sin\left[(Z_s\pm P_r)\theta_s\mp P_r\Omega t\right]$$

$$\Delta\varphi_{nP_r}=\left[\frac{1-c}{1+h_{pm}/(g\mu_r)}+\frac{\Lambda'_{s\min}/\Lambda_{s\min}-1/\left[1+h_{pm}/(g\mu_r)\right]}{(2-c)(\pi/Z_s)^2/2}\right]\frac{4F_m\sin(n\beta\pi)}{n\pi}$$

$$\Delta\varphi_{Z_s\pm P_r}=\left\{\begin{array}{l}\dfrac{\sin(\pi(1-c))}{1+h_{pm}/(g\mu_r)}+\dfrac{\Lambda'_{s\min}\sin(\pi c)(c-1)}{\Lambda_{s\min}c}\\-\dfrac{\sin(\pi c)(c-1)}{c+ch_{pm}/(g\mu_r)}+\dfrac{\cos(\pi c)-1}{\pi c}\end{array}\right\}\frac{4F_m\sin(\beta\pi)}{\pi^2}\tag{26}$$

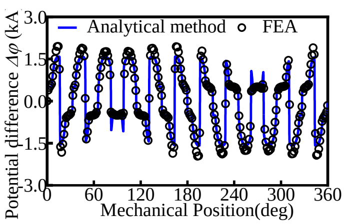

Fig. 24 Waveforms of $\Delta\varphi$ in SVPMM by FEA and oscillating $\Delta\varphi$ model.

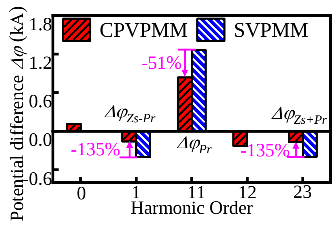

Fig. 25 Harmonic spectra of $\Delta\varphi$ of SVPMM and CPVPMM.

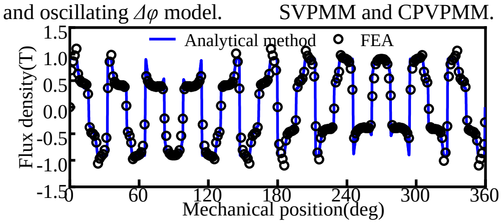

Fig. 26 Waveforms of B_g in SVPMM via FEA and oscillating $\Delta\varphi$ model.

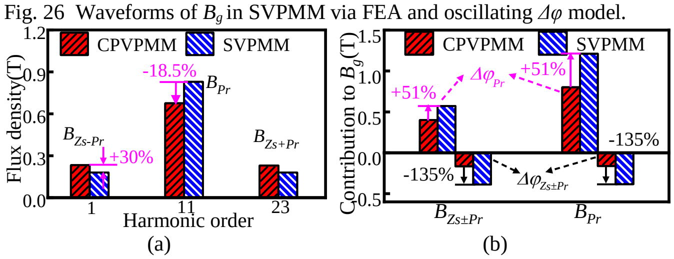

Fig. 27 Flux density harmonics of CPVPMM and SVPMM. (a) Harmonic spectra. (b) Generation of B_{Pr} and $B_{Zs\pm Pr}$ by $\Delta\varphi$ harmonics.

Owing to the $\Delta\varphi$-Λ_s analytical model, SVPMM has the same B_g expression as (22-a). Combine (22-a) and (26), the waveform of B_g in SVPMM is presented in Fig. 26 and agrees well with FEA result. Further, the harmonic spectra of B_g in SVPMM and CPVPMM is compared in Fig. 27(a), $B_{Zs\pm Pr}$ in CPVPMM is 30% larger than SVPMM, while B_{Pr} is only 18.5% smaller.

The difference could be explained by decomposing B_{Pr} and $B_{Zs\pm Pr}$ into component created by $\Delta\varphi_{Zs\pm Pr}$ and $\Delta\varphi_{Pr}$, as given in Fig. 27(b). Compared to CPVPMM, the positive B_{Pr} and $B_{Zs\pm Pr}$ created by $\Delta\varphi_{Pr}$ in SVPMM is 51% larger, however, the negative B_{Pr} and $B_{Zs\pm Pr}$ created by $\Delta\varphi_{Zs\pm Pr}$ is 135% larger. ***The negative $B_{Zs\pm Pr}$ outweighs the slight advantage in positive $B_{Zs\pm Pr}$, which makes $B_{Zs\pm Pr}$ in SVPMM much smaller than that of CPVPMM, while the improvement in B_{Pr} is quite limited.***

In Fig. 28, the waveform and harmonic spectra of E_a in two machines are calculated by the oscillating $\Delta\varphi$ model and FEA. E_1 of CPVPMM is 20.2% larger owing to 30% larger E_1 component induced by $B_{Zs\pm Pr}$ as shown in Fig.29(a). In Fig. 29(b), the contribution to E_1 by $\Delta\varphi$ harmonics in two machines are also given. For the major E_1 component induced by $B_{Zs\pm Pr}$, the offset ratio of negative E_1 induced by $\Delta\varphi_{Zs\pm Pr}$ is marked gray. It shows the negative E_1 in SVPMM offsets 70% of the positive one, while that in CPVPMM is only 42%. This explicitly explains why E_1 of SVPMM is smaller despite more magnets.

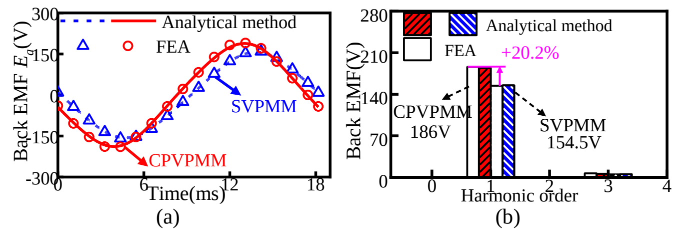

Fig. 28 E_a of SVPMM and CPVPMM. (a) Waveforms. (b) Harmonic spectra

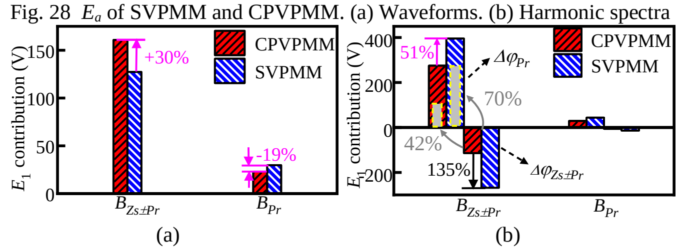

Fig. 29 E_1 composition in SVPMM and CPVPMM. (a) E_1 contributed by B_{Pr} and $B_{Zs\pm Pr}$. (b) E_1 contributed by $\Delta\varphi$ harmonics.

B. Torque Capability

The instantaneous torque T of CPVPMM and SVPMM can be generally expressed as (27), where T_{mag} is the electromagnetic torque as expressed in (24), T_{cog} is the cogging torque and T_{rel} is the reluctance torque.

$$T=T_{mag}+T_{cog}+T_{rel}\tag{27}$$

T_{rel} does not exist in SVPMM while T_{rel} is often ignored in CPVPMM due to the small ratio of L_q to L_d caused by the rotor anisotropic feature [20]. As a result, both machines can adopt the i_d=0 control strategy.

It is noted that as analyzed before, q axis would vary when saturation appears under loaded condition. Thus, the current initial phase should be adjusted accordingly.

When current density J is 2.1A/mm^2 at light load, the torque waveforms of two machines by FEA and analytical method are given in Fig. 30(a), where T_{cog} is FEA results. Good agreement between two methods validates the analytical method.

Further, the variations of torque density of two machines along with current density J are shown in Fig. 30(b), where the deviation between two methods in CPVPMM begins to increase when J exceeds 3.5A/mm^2. The reason is that iron core is more likely to saturate in CPVPMM due to the severer armature reaction, as shown in Fig. 31.

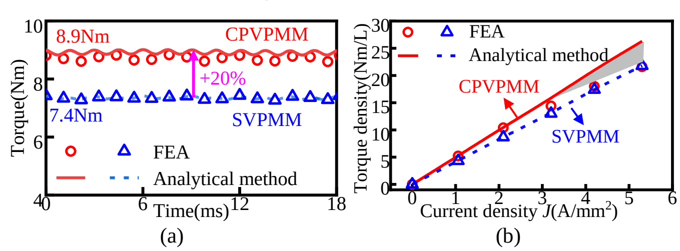

Fig. 30 Torque output of CPVPMM and SVPMM. (a) Torque waveforms by FEA and analytical methods. (b) Torque density variation with current density J.

This article has been accepted for publication in IEEE Transactions on Transportation Electrification. This is the author's version which has not been fully edited and content may change prior to final publication. Citation information: DOI 10.1109/TTE.2023.3301549

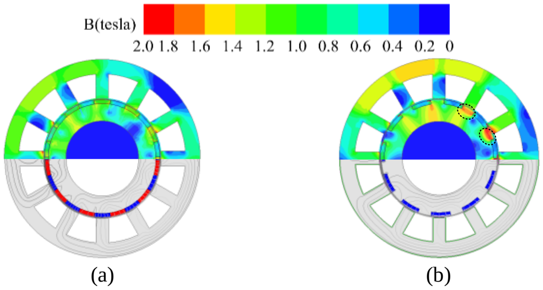

Fig. 31 Flux density contour plot of SVPMM and CPVPMM at I_m=2A. (a) SVPMM. (b) CPVPMM.

When rated current density is set as 4.2A/mm^2 (A=150A/cm) under natural cooling, the torque density of CPVPMM and SVPMM is 18.3Nm/L and 17.4Nm/L, respectively, while torque per magnet volume of two machines is 650.1Nm/L and 376.2Nm/L, separately. It indicates that CPVPMM has large torque capability and superior advantage in torque per magnet volume given the rising price of rare earth material.

C. Power Factor

Fig. 32 shows the vector diagram of VPMM. Under id=0 control and neglecting winding resistance, power factor (PF) of VPMM can be expressed as (28).

$$PF=\frac{E}{U}=\frac{E}{\sqrt{E^2+(\omega\psi_a)^2}}=\frac{1}{\sqrt{1+(\psi_a/\psi_{pm})^2}} \tag{28}$$

, where ψ_a and ψ_{pm} are armature and PM flux linkage, respectively. It is observed that PF is inversely proportional to ψ_a/ψ_{pm}. Thus, the key to restore PF is to analyze ψ_a.

Based on winding function, armature MMF F_a is given as:

$$\begin{aligned} &F_a(\theta_s,t)=F_w(\theta_s,t)+\Delta\varphi_a\\ &F_w(\theta_s,t)=\sum_{vP_a\neq 3k}^{\infty}F_{wv}\cos\left[vP_a\theta_s-\mathrm{sgn}(v)\omega t+\theta_{wv}\right]\\ &F_{wv}=3N_sI_mk_{wv}/(\pi vP_a),\Delta\varphi_a=\varphi_s-\varphi_r \end{aligned} \tag{29}$$

, where F_w is the MMF excited by the winding, sgn(v) and θ_{wv} reflects the rotation direction and initial phase of v^{th} MMF harmonic. $\Delta\varphi_a$ is the potential difference between stator core and rotor core under armature excitation, as shown in Fig. 33.

Similarly, if φ_s is assumed as 0, φ_r could be determined based on Gauss Theorem. φ_r in SVPMM and CPVPMM can be calculated as (30).

$$\begin{aligned} &\varphi_{r\_svpmm}=0\\ &\varphi_{r\_cpvpmm}=F_{wP_r}\lambda_{r1}/(2\lambda_{r0})+F_{wP_a}\lambda_{s1}\lambda_{r1}/(4\lambda_{r0}\lambda_{s0}) \end{aligned} \tag{30}$$

, where $\varphi_r \neq 0$ in CPVPMM and would have impact on armature flux density.

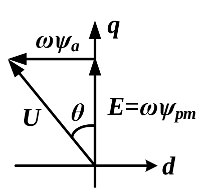

Fig. 32 Vector diagram of power factor of PM machine.

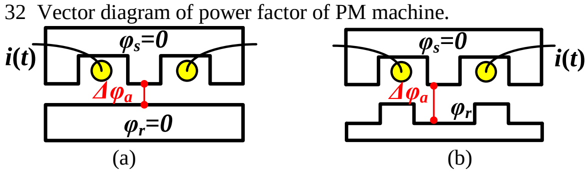

Fig. 33 Potential difference $\Delta\varphi_a$ in two VPMMs. (a) SVPMM. (b) CPVPMM.

Similarly, armature flux density B_a in two machines can be calculated as (31) and (32), respectively. ***It is observed that $\Delta\varphi_a$ in CPVPMM would also undermine B_{a1} and $B_{aPr/Pa}$.***

$$\begin{aligned} B_{a\_svpmm}(\theta_s,t)&=F_a(\theta_s,t)\Lambda_s(\theta_s)\\ &=\sum F_{av}\Lambda_{s0}\cos(vP_a\theta_s-\mathrm{sgn}(v)\omega t+\theta_{wv})\\ &+\sum 0.5F_{av}\Lambda_{s1}\cos((vP_a\pm Z_s)\theta_s-\mathrm{sgn}(v)\omega t+\theta_{wv}) \end{aligned} \tag{31}$$

$$\begin{aligned} B_{a\_cpvpmm}(\theta_s,t)&=F_a(\theta_s,t)\Lambda_{sr}(\theta_s)\\ &\approx\sum g/\mu_0\,F_{av}\Lambda_{r0}\Lambda_{s0}\cos(vP_a\theta_s-\mathrm{sgn}(v)\omega t+\theta_{wv})\\ &+\sum g/\mu_0\,F_{av}\Lambda_{s1}\Lambda_{r0}\cos((vP_a\pm Z_s)\theta_s-\mathrm{sgn}(v)\omega t+\theta_{wv})\\ &-\Delta\varphi_a g/\mu_0\begin{bmatrix}\Lambda_{r0}\Lambda_{s0}\cos(P_r\theta_s-\omega t+\theta_{wP_r})\\ +0.5\Lambda_{r1}\Lambda_{s1}\cos(P_a\theta_s+\omega t+\theta_{wP_r})\end{bmatrix} \end{aligned} \tag{32}$$

Then, ψ_a in two machines can be calculated as (33) and (34), where the higher order F_{av}, the less contribution to ψ_a. Moreover, $\Delta\varphi_a$ undermines ψ_a in CPVPMM.

$$\Psi_{a\_svpmm}=2N_sr_gL\left(\sum_{vP_a}\frac{F_{av}\Lambda_{s0}}{vP_a}k_{wv}+\sum_{vP_a\pm Z_s}\frac{0.5F_{av}\Lambda_{s1}}{vP_a\pm Z_s}k_{wv\pm\frac{Z_s}{P_a}}\right) \tag{33}$$

$$\Psi_{a\_cpvpmm}=\frac{2N_sgr_gL}{\mu_0}\left(\begin{aligned}&\sum_{vP_a}\frac{F_{av}\Lambda_{s0}\Lambda_{r0}}{vP_a}k_{wv}+\sum_{vP_a\pm Z_s}\frac{F_{av}\Lambda_{s1}\Lambda_{r0}}{vP_a\pm Z_s}k_{wv\pm\frac{Z_s}{P_a}}\\ &-\frac{\Delta\varphi_a\Lambda_{s0}\Lambda_{r0}}{P_r}k_{w\frac{P_r}{P_a}}-\frac{\Delta\varphi_a\Lambda_{s1}\Lambda_{r1}}{2P_a}k_{w1}\end{aligned}\right) \tag{34}$$

Based on (33) and (34), the detailed major armature flux density harmonics and induced flux linkage at J=2.1A/mm^2 are analyzed, as presented in Table IV, while the power factor comparison is presented in Table V.

TABLE IV
ARMATURE FLUX DENSITY HARMONICS AND FLUX LINKAGE

SVPMM							
B_{av} and induced ψ_a				Major Source			
				Armature MMF		Permenace	
v	B_v/T	θ_{wv}/°	ψ_a/wb	v	value/A	j	value/mH
1	**0.1**	**0**	**0.2**	**1**	**378∠0°**	**0**	**0.27∠0°**
				11	**16∠180°**	**12**	**0.14∠0°**
5	0	-	-	5	66∠0°	0	0.27∠0°
7	0	-	-	7	41∠180°	0	0.27∠0°
11	0.04	0	0.003	11	16∠180°	0	0.27∠0°
				1	378∠0°	12	0.14∠0°
13	0.02	0	0.001	13	9∠0°	0	0.27∠0°
Total ψ_a (wb)				Analytical		FEA	
				0.2		0.22	
CPVPMM							
B_{av} and induced ψ_a				Major Source			
				Armature MMF		Permenace	
v	B_v/T	θ_{wv}/°	ψ_a/wb	v	value/A	j	value/mH
1	**0.21**	**0**	**0.428**	**1**	**378∠0°**	**0**	**0.6∠0°**
				11	**16∠180°**	**12**	**0.5∠0°**
				$\Delta\varphi_a$	**84.5∠0°**	**1**	**0.2∠180°**
5	0.01	180	-0.004	5	66∠0°	0	0.6∠0°
7	0.01	180	-0.002	7	41∠180°	0	0.6∠0°
11	0.1	0	0.008	11	16∠180°	0	0.6∠0°
				1	378∠0°	12	0.5∠0°
				$\Delta\varphi_a$	84.5∠0°	11	0.4∠180°
13	0.08	0	0.004	13	9∠0°	0	0.6∠0°
Total ψ_a (wb)				Analytical		FEA	
				0.43		0.44	

TABLE V
FLUX LINKAGE COMPONENTS AND POWER FACTOR IN TWO MACHINES

Machine type	Armature flux linkage (wb)	PM flux linkage (wb)	Power Factor
SVPMM	0.22	0.44	0.89
CPVPMM	0.44	0.54	0.78

It is found that B_{a1} mainly induces ψ_a in both machines. ***Moreover, F_{a11} undermines B_{a1}, while $\Delta\varphi_a$ also undermines B_{a1} in CPVPMM which is good for improving PF.*** However, Λ_0 and Λ_{12} in CPVPMM is much larger than that of SVPMM due to smaller equivalent airgap length, thus B_{a1} in CPVPMM is twice that of SVPMM, and leads to smaller *PF*.

As the major parameter h_{pm} would impact $\Delta\varphi_a$ which in return influences *PF* of CPVPMM, the effect of h_{pm} on both torque and *PF* are analyzed in analytical and FEA methods, as shown in Fig. 34. Despite saturation effect, both *PF* and average torque enhances as h_{pm} increases. Besides, iron saturation has larger effect on reducing B_a, thus *PF* will be larger than the analytical result. ***Hence, large h_{pm} is very suitable for CPVPMM.***

Finally, the torque and *PF* variations along with *J* of SVPMM with β=0.5, h_{pm}=2.5mm and CPVPMM with β=0.6, h_{pm}=4.2mm (same magnet usage) are compared in Fig. 35, indicating that CPVPMM has almost 20% larger torque density and similar *PF* as SVPMM at light load.

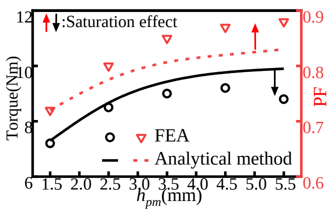

Fig. 34 Variation of torque and power factor along with h_{pm}.

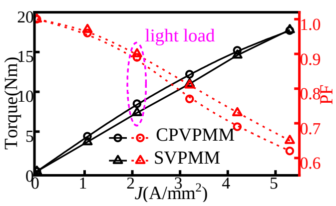

Fig. 35 Torque and *PF* variation along with current density *J*.

D. Relationship between CPVPMM and SVPMM

It is now revealed that $\Delta\varphi$ oscillation undermines the torque output, which indicates that CPVPMM can be regarded as the improvement of SVPMM in regard of structure.

To illustrate, $\Delta\varphi$ of SVPMM is qualitatively plotted in Fig.36, where $\Delta\varphi$ oscillation appears on the surface of both *N* and *S* magnet array due to the oscillating flux in each magnet caused by the slotted stator, thus $\Delta\varphi_{Zs\text{-}Pr}$ in SVPMM comes from two sets of magnet arrays. Hence, it is rational to think about restraining $\Delta\varphi_{Zs\text{-}Pr}$ via retaining the flux that passes the magnetic pole.

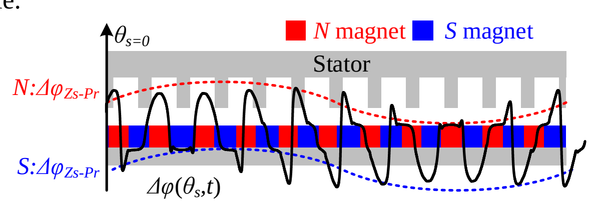

Fig. 36 Illustration of oscillating $\Delta\varphi$ of SVPMM.

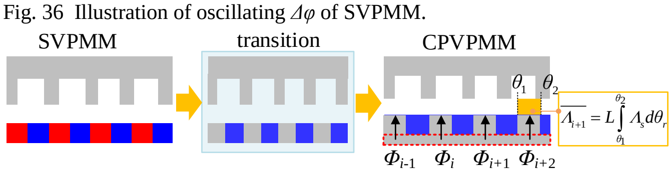

Fig. 37 Evolution from SVPMM to CPVPMM.

As plotted in Fig.37, half magnets of same polarity in SVPMM are replaced with ferromagnetic poles, which are passive magnetic pole and their magnetic potential are decided by the corresponding flux circuit. Then, all the ferromagnetic poles are connected by the rotor core to form one magnetic pole, of which the potential φ_r could be analyzed by (35).

$$\varphi_r = \sum_{i=1,2...}^{P_r} \Phi_{ri}(\theta_s,t) \Big/ \sum_{i=1,2...}^{P_r} \overline{\Lambda}_{ri}(\theta_s,t) \tag{35}$$

, where $\Phi_{ri}(\theta_s, t)$ is the flux passing the i^{th} rotor pole and $\overline{\Lambda}_{ri}(\theta_s,t)$ is the lumped permeance above i^{th} rotor pole as shown in Fig.37. Because of the stator slotting effect, the amplitude variation of $\Phi_{ri}(\theta_s,t)$ and $\overline{\Lambda}_{ri}(\theta_s,t)$ repeats once rotor rotates a stator pole arc [22]. Thus, $\Phi_{ri}(\theta_s,t)$ and $\overline{\Lambda}_{ri}(\theta_s,t)$ could be presented as (36).

$$\begin{aligned} \Phi_{ri}(\theta_s,t) &= \Phi_{r0} + \Phi_{r1}\cos(Z_s(\theta_s - \Omega t) + i\,2\pi/Z_s) \\ \overline{\Lambda}_{ri}(\theta_s,t) &= \overline{\Lambda}_{r0} - \overline{\Lambda}_{r1}\cos(Z_s(\theta_s - \Omega t) + i\,2\pi/Z_s) \end{aligned} \tag{36}$$

, where Φ_{r0} and Φ_{r1} is the amplitude of constant and fundamental harmonic of Φ_{ri}. $\overline{\Lambda}_{r0}$ and $\overline{\Lambda}_{r1}$ is the amplitude of constant and fundamental harmonic of $\overline{\Lambda}_{ri}$.

Put (35) into (36), it is found that fundamental harmonic of Φ_{ri} and $\overline{\Lambda}_{ri}$ in P_r rotor poles cancel out each other and (35) becomes (37) where φ_r is almost constant when rotor rotates, indicating that $\Delta\varphi_{Zs\text{-}Pr}$ is only from one magnet array.

$$\varphi_r = \Phi_{r0} \big/ \overline{\Lambda}_{r0} \tag{37}$$

As a result, the amplitude of undesired $\Delta\varphi_{Zs\text{-}Pr}$ in CPVPMM is at least half of that in SVPMM, thus leading to larger working flux density. ***In other words, CPVPMM gives better play to the flux modulation effect due to consequent pole structure, which helps to exploit the torque potential in VPMM.***

VII. EXPERIMENTAL VALIDATION

Based on the given design hints, a 12slots20poles CPVPMM was manufactured with the structure parameters listed in Table VI to validate the analysis above. The machine assembly and test platform setup are presented in Fig. 38.

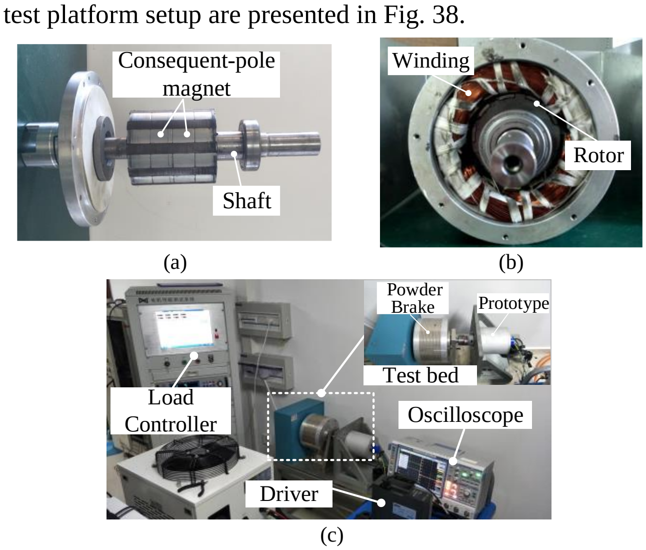

Fig. 38 Machine assembly and test platform. (a) Consequent-pole rotor. (b) Cross section view of prototype. (c) Test platform setup.

TABLE VI
PARAMETERS OF CPVPMM PROTOTYPE

Parameter	Value	Parameter	Value
Stator outer diameter	124mm	Air-gap length	0.8mm

This article has been accepted for publication in IEEE Transactions on Transportation Electrification. This is the author's version which has not been fully edited and content may change prior to final publication. Citation information: DOI 10.1109/TTE.2023.3301549

Stator inner diameter	76mm	Stack length	80mm
Magnet thickness	3.5mm	PM Pole arc ratio	0.6
Serial turn number	120	Slot open ratio	0.6

The platform includes the magnetic powder brake, prototype, driver, current sensor, load controller, and oscilloscope, where the magnetic powder brake worked as the load and is driven by the load controller. The average torque can be measured according to the value shown on the load controller. At the same time, the phase voltage and current can be tested and shown by the oscilloscope, and used to measure the machine power factor.

Firstly, the open-circuit phase back EMF waveform at rotation speed 300rpm was tested as depicted in Fig. 39, where the analysis, FEA and measured results have good agreement.

Then, the loaded performances are investigated. Considering winding inductance has small variation with rotor rotation, i_d=0 control has been adopted. The average torque versus current characteristic for the prototype are measured and compared with analytical and FEA results in Fig. 40(a). High agreement between three methods are observed, except that iron core becomes saturated when current exceeds 8A, and error between analytical result and measured one begins to increase.

Fig. 40(b) shows the measured phase current/voltage waveforms at the current I_{rms}=10A. It can be seen that the phase angle difference between voltage and current is 53° and the *PF* is then obtained as 0.6, which reflects the low *PF* of CPVPMM brought by the large inductance under CP structure.

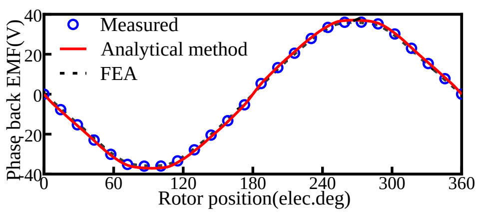

Fig. 39 Phase back EMF waveforms at rated speed 300rpm.

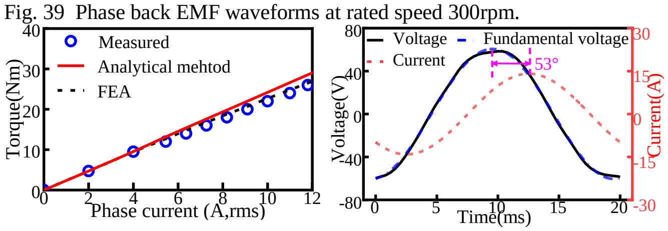

(a) (b)

Fig. 40 Loaded performances. (a) Average torque versus phase current. (b) Measured phase voltage/current waveforms.

VIII. Conclusions

In this paper, a new analytical model i.e. the oscillating magnetic potential difference $\Delta\varphi$ between stator core and rotor surface is proposed to comprehend the working mechanism of CPVPMM. The main conclusions of the paper are as followed.

1) The mostly-used simplified Λ_{sr} model is invalidated in CPVPMM due to the inaccurate interpretation of air gap flux density harmonics. Moreover, the simplified Λ_{sr} would miss the physical phenomenon of oscillating $\Delta\varphi$, thus losing the vital information of additional time-space harmonics $\Delta\varphi_{Zs\pm Pr}$.

2) $\Delta\varphi_{Zs\pm Pr}$ reduces working flux density, and influences the E_1 composition in CPVPMM to different extent depending on PR. Thus, $\Delta\varphi_{Zs\pm Pr}$ is of vital importance to understanding the working mechanism of CPVPMM.

3) The stator and rotor structure parameters are separately studied based on the proposed $\Delta\varphi$ model, while the core saturation is also considered. It is found that when magnet thickness is large and pole arc ratio is around 0.6, CPVPMM can obtain large torque output and power factor at the same time.

4) Based on the proposed $\Delta\varphi$ model, both CPVPMM and SVPMM has $\Delta\varphi_{Pr}$ and $\Delta\varphi_{Zs\pm Pr}$. However, CPVPMM has 135% smaller $\Delta\varphi_{Zs\pm Pr}$ while $\Delta\varphi_{Pr}$ is only 51% smaller than SVPMM owing to the CP magnet structure, thus acquiring larger flux density and torque capability. In this means, CP magnet gives better play to the flux modulation effect by restraining $\Delta\varphi_{Zs\pm Pr}$, which gives clue to exploiting the torque capability of VPMM.

5) The potential oscillation induced by the dual-salient air gap could reduce armature reaction, thus improving power factor of CPVPMM to some extent. Besides, both power factor and torque enhance as h_{pm} increases, which further proves that thick magnet is very suitable for CPVPMM.

In the future, the research will involve the analysis and design of rotors with different CP structures. Besides, the reluctance torque in CPVPMM with medium/low PR also contributes to torque, and is closely related to the CP rotor structure. Thus, how to design the CP rotor to restrain the iron saturation and exert the reluctance torque is of vital importance. In this means, the proposed analytical model lays the foundation for accurately studying the flux density distribution and torque generation of CPVPMM.

IX. Appendix

Based on the analysis in Fig. 4, the feature value of k_λ at λ_r =1 and λ_{rmin} is firstly obtained, which is k_λ=1 and $1/(\lambda_{rmin}+\lambda_s-\lambda_{rmin}\lambda_s)$. Further, $k_\lambda(\lambda_r=\lambda_{rmin})$ is expressed as the function of λ_s. Then, λ_s at 1, $(1+\lambda_{smin})/2$ and λ_{smin} are selected, and the feature values of $k_\lambda(\lambda_r=\lambda_{rmin})$ are obtained as (38).

$$\frac{1}{\lambda_{rmin}+\lambda_s-\lambda_{rmin}\lambda_s}=\begin{cases}1, \lambda_s=1\\ 2/\left(\lambda_{rmin}+\lambda_{smin}-\lambda_{rmin}\lambda_s+1\right), \lambda_s=\dfrac{1+\lambda_{smin}}{2}\\ 1/\left(\lambda_{rmin}+\lambda_{smin}-\lambda_{rmin}\lambda_{smin}\right), \lambda_s=\lambda_{smin}\end{cases} \tag{38}$$

, where λ_{smin} is minimum value of λ_s.

Then, the equivalent quadratic function of $k_\lambda(\lambda_r=\lambda_{rmin})$ about λ_s is obtained by three-point formula, and expressed as (39).

$$\begin{aligned}
&k_\lambda(\lambda_r=\lambda_{rmin})=k_1\lambda_s^2+k_2\lambda_s+k_3\\
&k_1=\frac{2}{(1-\lambda_{smin})^2}\left(1-\frac{4}{k+1}+\frac{1}{k}\right)\\
&k_2=-\frac{1}{(1-\lambda_{smin})^2}\left[3\lambda_{smin}+1-\frac{8\left(\lambda_{smin}+1\right)}{k+1}+\frac{\lambda_{smin}+3}{k}\right]\\
&k_3=\frac{1}{(1-\lambda_{smin})^2}\left[\left(\lambda^2{}_{smin}+\lambda_{smin}\right)-\frac{8\lambda_{smin}}{k+1}+\frac{\lambda_{smin}+1}{k}\right]\\
&k=\lambda_{smin}+\lambda_{rmin}-\lambda_{smin}\lambda_{rmin}
\end{aligned} \tag{39}$$

Finally, (39) transforms to (15) to suit k_λ (λ_r=1) as well. Relative permeance-related coefficient A_1-A_6 is given as:

$$
\begin{aligned}
A_1 &= \frac{\lambda_{r1}\lambda_{r\min}(k_1\lambda^2_{s0}+k_2\lambda_{s0}+k_3+\frac{k_1\lambda^2_{s1}}{2})-\lambda_{r1}}{1-\lambda_{r\min}} \\
A_2 &= \frac{\lambda_{r\min}\lambda_{r1}\lambda_{s1}(2k_1\lambda_{s0}+k_2)}{2(1-\lambda_{r\min})} \\
A_3 &= \frac{\lambda_{r\min}(1-\lambda_{r0})(k_1\lambda^2_{s0}+k_2\lambda_{s0}+k_3+\frac{k_1\lambda^2_{s1}}{2})+(\lambda_{r0}-\lambda_{r\min})}{1-\lambda_{r\min}} \\
A_4 &= \frac{\lambda_{r\min}(1-\lambda_{r0})\lambda_{s1}(2k_1\lambda_{s0}+k_2)}{1-\lambda_{r\min}} \\
A_5 &= \frac{\lambda_{r2}[\lambda_{r\min}(k_1\lambda^2_{s0}+k_2\lambda_{s0}+k_3+\frac{k_1\lambda^2_{s1}}{2})-1]}{1-\lambda_{r\min}} \\
A_6 &= \frac{\lambda_{r\min}\lambda_{r2}(2k_1\lambda_{s0}\lambda_{s1}+k_2\lambda_{s1})}{2(1-\lambda_{r\min})}
\end{aligned} \tag{40}
$$

X. Acknowledgement

This work was supported in part by the National Key Laboratory of Electromagnetic Energy under Grant 61422172220101, and in part by the National Natural Science Foundation of China (NSFC) under Grant 51991382 and 52122705.

XI. References

[1] C. Liu, "Emerging electric machines and drives–An overview," IEEE Trans. Eng. Convers., vol, 33, no. 4, pp. 2270–2280, Dec. 2018.

[2] G. Zhang, W. Hua, M. Tong, etc., "Design and Manufacturing Considerations of Flux-Switching Permanent Magnet Motors for Mass Productions used in EVs and HEVs," i*n 18th Int. Conf. Elect. Mach. Sys.*, Thailand, 2015.

[3] D. Li, R. Qu, J. Li, L. Wu, and W. Xu," Analysis of Torque Capability and Quality in Vernier Permanent-Magnet Machines," *IEEE Trans. Ind. Appl.*, vol.52, no.1, pp.125-135, Jan./Feb.2016.

[4] K. Du, L. Xu, W. Zhao, G. Liu, "Analysis and Design of a Fault-Tolerant Permanent Magnet Vernier Machine With Improved Power Factor," *IEEE Trans. Ind. Electron.*, vol.69, no.5, pp. 4353-4363, May. 2022.

[5] A. Ishizaki, T. Tanaka, K. Takasaki, and S. Nishikata, "Theory and Optimum Design of PM Vernier Motor," *in Proc. Int. Conf. Elect. Mach. Drives*, UK, 1995.

[6] B. Kim, T. Lipo, "Operation and Design Principles of a PM Vernier Motor," *IEEE Trans. Ind. Appl.*, vol. 50, no.6, pp. 3656-3663, Nov./Dec. 2014.

[7] L Fang, D Li, X Ren and Qu R, "A Novel Permanent Magnet Vernier Machine With Coding-Shaped Tooth". *IEEE Trans. Ind. Electron.*, vol.69, no.6, pp: 6058-6068, June 2022.

[8] S. U. Chung, S.H. Moon, D.J. Kim, and J.M. Kim, "Development of a 20-pole–24-slot SPMSM with Consequent Pole Rotor for In-wheel Direct Drive," *IEEE Trans. Ind. Electron.*, vol. 63, no. 1, pp. 302–309, Jan. 2016.

[9] X. X. Liu, C. H. Zou, Y. Du, F. Xiao, "A Linear Consequent-Pole Stator Permanent Magnet Vernier Machine," *in 17th Int. Conf. Elect. Mach. Sys.*, China, 2014.

[10] Z. Zhu, Y. Pang, D. Howe, S. Iwasaki, etc., "Analysis of Electromagnetic Performance of Flux-Switching Permanent Magnet Machines by Nonlinear Adaptive Lumped Parameter Magnetic Circuit Model," *IEEE Trans. Magn.*, vol.41, no.11, pp.4277–4287, Nov. 2005.

[11] L. Jian, G. Xu, C. C. Mi, K. T. Chau, etc., "Analytical Method for Magnetic Field Calculation in a Low-Speed Permanent-Magnet Harmonic Machine," *IEEE Trans. Energy Convers.*, vol. 26, no. 3, pp. 862–870, Sep. 2011.

[12] D. Zarko, D. Ban, and T. A. Lipo, "Analytical calculation of magnetic field distribution in the slotted air gap of a surface permanent-magnet motor using complex relative air-gap permeance," *IEEE Trans. Magn.*, vol. 42, no. 7, pp. 1828–1837, Jul. 2006.

[13] A. Toba, T. A. Lipo, "Generic Torque-Maximizing Design Methodology of Surface Permanent-Magnet Vernier Machine," *IEEE Trans. Ind. Appl.*, vol. 36, no.6, pp.1539-1546, Nov./Dec. 2000.

[14] L. J. Wu, Z. Q. Zhu, David. A. Staton, etc., "Comparison of Analytical Models of Cogging Torque in Surface-Mounted PM Machines," *IEEE Trans. Ind. Electron*., vol. 59, no. 6, pp. 2414-2425, June 2012.

[15] H. Yang, Z. Q. Zhu, H. Lin, H. Li and S. Lyu, "Analysis of Consequent-Pole Flux Reversal Permanent Magnet Machine With Biased Flux Modulation Theory," *IEEE Trans. Ind. Electron*., vol. 67, no. 3, pp.2107-2121, March 2019.

[16] B. Heller and V. Hamata, "Harmonic Field Effects in Induction Machines", *Elsevier Scientific Publishing Co.*, Amsterdam, 1977.

[17] L. Fang, D. Li, R. Qu., "Torque Improvement of Vernier Permanent Magnet Machine with Larger Rotor Pole Pairs than Stator Teeth Number," *IEEE Trans. Ind. Electron.*, vol. 70, no. 12, pp. 12648-12659, Dec. 2023.

[18] Y. Zhang, D. Li, P. Yan, X. Ren, et al. "A High Torque Density Claw Pole-Permanent Magnets Vernier Machine". *IEEE Jour. Emer. Select. Topics in Pow. Electron.*, vol.10, no.2, pp: 1756-1765, April 2022.

[19] T. Zou, "Research on Theory and Topologies of High Performance Flux Modulation Permanent Magnet Machines," *Doctoral Thesis*, Huazhong University of Science and Technology, China, 2018.

[20] D. Li, R. Qu and T. A. Lipo, "High-Power-Factor Vernier Permanent-Magnet Machines," *IEEE Trans. Ind. Appl.*, vol. 50, no. 6, pp. 3664-3674, Nov./Dec. 2014.

[21] Z. Q. Zhu and Y. Liu, "Analysis of Air-Gap Field Modulation and Magnetic Gearing Effect in Fractional-slot Concentrated-Winding Permanent-Magnet Synchronous Machines," *IEEE Trans. Ind. Electron.* vol. 65, no. 5, pp. 1320-1330. Mar. 2018.

[22] B. Kim, T. Lipo, "Operation and Design Principles of a PM vernier motor," *IEEE Trans. Ind. Appl.*, vol. 50, no.6, pp. 3656-3663, Nov./Dec. 2014.

Li Fang received her B.E.E. degree in electrical engineering in 2018 from the Huazhong University of Science and Technology, Wuhan, China, where she is currently working toward the Ph. D degree in electrical engineering. Her major research interests include design and analysis of novel magnetic field modulation permanent magnet machines.

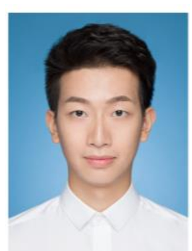

Yuanzhi Zhang (Member, IEEE) received his B.E.E. degree and Ph. D degree in electrical engineering from the Huazhong University of Science and Technology, Wuhan, China in 2017 and 2022, respectively. He is currently a postdoc with Wuhan University. His research interests include analysis and design of novel permanent magnet brushless machines and superconducting machines.

Dawei Li (Senior Member, IEEE) received his B.E.E. degree from the Harbin Institute of Technology, Harbin, China, in 2010 and the Ph. D degree from the Huazhong University of Science and Technology, Wuhan, China, in 2015, both in electrical engineering. In 2015, he joined the Huazhong University of Science &Technology. His research areas include the design and analysis of servo motors, high-power electric machines and flux modulation permanent-magnet machines.

This article has been accepted for publication in IEEE Transactions on Transportation Electrification. This is the author's version which has not been fully edited and content may change prior to final publication. Citation information: DOI 10.1109/TTE.2023.3301549

Tianjie Zou (Member, IEEE) received his B.E.E and Ph. D degree in electrical engineering from the Huazhong University of Science and Technology, Wuhan, China, in 2013 and 2018, respectively. He is now a research fellow at the Power Electronics, Machines and Control Group, University of Nottingham. His research interests include the design, analysis and intelligent control of permanent magnet machines.